UC San Diego
UC San Diego Previously Published Works

Title

Hot Neutron Star Matter and Proto-neutron Stars

Permalink

ISBN

Authors

Farrell, Delaney
Alp, Aksel
Weber, Fridolin
et al.

Publication Date

DOI

Copyright Information

Peer reviewed

Chapter 1

Hot Neutron Star Matter and Proto Neutron Stars

Delaney Farrell[†], Aksel Alp[‡]

Department of Physics, San Diego State University, 5500 Campanile Drive, San Diego, CA 92182, USA
Email: [†] dfarrell@sdsu.edu, [‡] aalp@sdsu.edu

Fridolin Weber

Department of Physics, San Diego State University, 5500 Campanile Drive, San Diego, CA 92182, USA
Center for Astrophysics and Space Sciences, University of California at San Diego, La Jolla, CA 92093, USA
Email: fweber@sdsu.edu, fweber@ucsd.edu

William Spinella

Department of Physical Sciences, Irvine Valley College, Irvine Center Drive, Irvine, CA 92618, USA
Email: wspinella@ivc.edu

Germán Malfatti

Grupo de Gravitación, Astrofísica y Cosmología, Facultad de Ciencias Astronómicas y Geofísicas, Universidad Nacional de La Plata, Paseo del Bosque S/N, La Plata (1900), Argentina
Email: gmalfatti@fcaglp.unlp.edu.ar

Milva G. Orsaria[*], Ignacio F. Ranea-Sandoval[**]

Grupo de Gravitación, Astrofísica y Cosmología, Facultad de Ciencias Astronómicas y Geofísicas, Universidad Nacional de La Plata, Paseo del Bosque S/N, La Plata (1900), Argentina
Consejo Nacional de Investigaciones Científicas y Técnicas (CONICET), Godoy Cruz 2290, Buenos Aires (1425), Argentina

Email: *morsaria@fcaglp.unlp.edu.ar,* ***iranea@fcaglp.unlp.edu.ar*

Abstract: In this chapter, we investigate the structure and composition of hot neutron star matter and proto-neutron stars. Such objects are made of baryonic matter that is several times denser than atomic nuclei and tens of thousands times hotter than the matter in the core of our Sun. The relativistic finite-temperature Green function formalism is used to formulate the expressions that determine the properties of such matter in the framework of the density-dependent mean field approach. Three different sets of nuclear parametrizations are used to solve the many-body equations and to determine the models for the equation of state of ultra-hot and dense stellar matter. The meson-baryon coupling scheme and the role of the $\Delta(1232)$ baryon in proto-neutron star matter are investigated in great detail. In addition, using the non-local three-flavor Nambu—Jona-Lasinio model to describe quark matter, the hadron-quark composition of dense baryonic matter at zero temperature is discussed briefly. General relativistic models of non-rotating as well as rotating proto-neutron stars are presented in part two of our study.

Contents

1.1   Introduction

Within a few million years after a massive star ($\gtrsim 8\,M_\odot$) is born, its core undergoes nuclear fusion reactions that will result in a dense, heavy iron center. Up until the formation of an iron core, the massive star has been supported from collapsing by the energy released from fusing lighter elements into iron and electron degeneracy pressure (Mezzacappa, 2005; Janka, 2012; Foglizzo, 2016; Burrows and Vartanyan, 2021). When an iron core is formed, the fusion processes and subsequent energy cease; at this point, the star can no longer support its mass against the force of gravity and will begin to rapidly collapse in the span of just a few milliseconds. At this moment, the core's temperature skyrockets and the density surpasses the point of electron degeneracy, sparking the formation of neutrons through electron capture,

$$p + e^- \rightarrow n^0 + \nu_e\,, \tag{1.1}$$

where p, a proton, and e^-, an electron, combine to form a neutron, n^0, and an electron neutrino, ν_e. These neutrinos are released carrying large quantities of energy, contracting the core further. The density of the core increases until it reaches nuclear density (baryon number density of around $0.16\,\mathrm{fm}^{-3}$, mass density of or $2.65 \times 10^{14}\,\mathrm{g/cm}^3$), where nucleon degeneracy pressure halts the collapse. Parts of the core surpassing nuclear density, like the inner most part of the core, will rebound to create a shock wave as the exterior core layers are expelled. Over the next tens of seconds, the shock wave reverses the inward trajectory of the collapsing stellar material as it moves through the stellar envelope, partially cooling the extreme temperature and contracting the material it passes through. The shock wave alone does not possess enough energy to pass through the entire stellar envelope and complete the supernova explosion; the shock wave is revived by the massive quantities of neutrinos created alongside neutrons. While most neutrinos are expelled, some remain trapped behind the shock wave, increasing the pressure and pushing the wave outward (Camelio *et al.*, 2017). This portion of the star's collapse is referred to as the Kelvin-Helmholtz phase, and the contracting core during this phase is called a proto-neutron star (PNS) (Prakash *et al.*, 1997; Pons *et al.*, 1999; Strobel *et al.*, 1999; Camelio *et al.*, 2017). Depending on the final mass of the core after the short-lived life of a PNS, a black hole or neutron star (NS) is left behind. This chapter will focus on the structure and evolution of the compact stellar objects (proto-neutron stars) produced by the collapse of massive ($8\,M_\odot$ to around $20\,M_\odot$) stars.

The macroscopic evolution of the PNS during the Kelvin-Helmholtz phase, where a hot, lepton-rich PNS turns into a cold, deleptonized neutron star (Weber, 1999, 2005; Sedrakian, 2007; Becker, 2009; Glendenning, 2012; Rezzolla *et al.*, 2019; Orsaria *et al.*, 2019), is dependent on the microphysical ingredients of the star, the equation of state (EOS) of the dense matter comprising the core, and neutrino opacity (Pons *et al.*, 1999). Immediately (in a matter of 0.1 to 0.5 seconds) following the core bounce during a massive star's collapse and just prior to the Kelvin-Helmholtz phase, the PNS radius rapidly decreases from over 150 km to less than 20 km as pressure decreases as a result of neutrinos being released from the outer envelope of the star (Pons *et al.*, 1999). While the star's original matter rapidly compresses, the supernova's shock causes accretion which results in a substantial increase in mass and total neutrino emission. These conditions make it so the copious amount of neutrinos cannot escape freely, and instead diffuse over the course of about a minute (the deleptonization stage) while a large fraction of the gravitational binding energy is released during the contraction of the stellar envelope (Foglizzo, 2016). After this minute-long period, neutrinos can escape freely, and the PNS enters a cooling stage where the entropy steadily decreases (Pons *et al.*, 1999). The completion of the deleptonization and cooling stages signifying the end of the Kelvin-Helmholtz phase and the beginning of the life of a neutron star.

The different stages in the evolution of hot proto-neutron stars to cold neutron stars, as described above, is schematically illustrated in Fig. 1.1. Proto-neutron stars are the compact remnants produced at the end of the evolution of intermediate-mass stars with masses of $M \gtrsim 10 M_\odot$ (see Mariani (2020), and references therein). Their structure and composition passes through different physical stages within just a few seconds (see, for example, Prakash *et al.* (1997); Pons *et al.* (1999)). Stars with $M \gtrsim 10 M_\odot$ are known to evolve in a complex fashion via nuclear burning. At the end of their lives, when most of the nuclear fuel has been consumed and massive cores of Fe (or O-Ne/Mg) have been built up, gravitational collapse occurs. During this phase (stage "1" in Fig. 1.1) a rebound of the outer mantle of the star occurs. The core is surrounded by a mantle characterized by low density but high entropy of the matter. The mantle extends for around 200 km and is stable until it explodes due to the aforementioned rebound. At this point, two different evolutionary tracks of the star are possible, which essentially depend on how powerful the explosion was. If the explosion was not strong enough to deleptonize the outer mantle, continued accretion of matter onto the star would give way to the formation of a
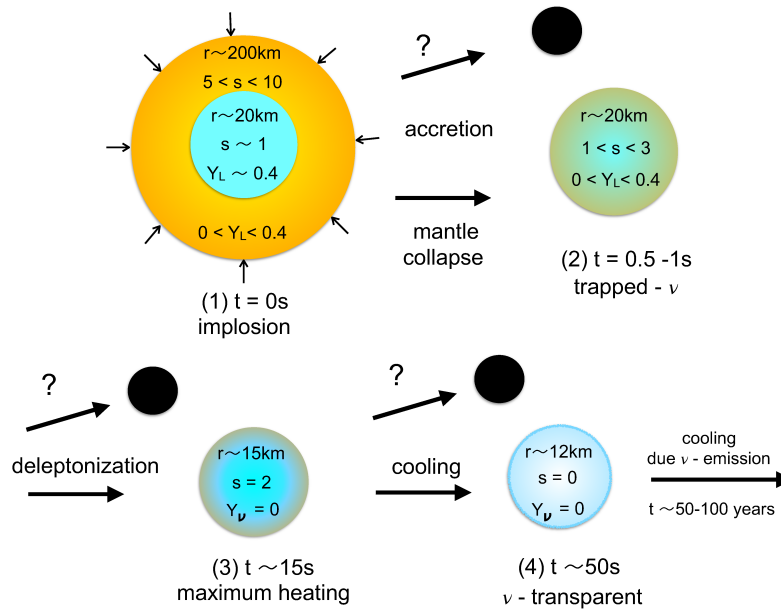
Fig. 1.1   Schematic illustration of different temporal stages in the evolution of proto-neutron stars to neutron stars [Prakash *et al.* (1997)]. They are characterized by different values of entropy (s) and lepton number (Y_L). The formation of black holes (solid black spheres) is possible during different evolutionary stages, depending on the interplay between gravity and pressure. The transition of a hot PNS to a cold NS takes less than a minute. During the first few hundred years NSs cool quickly via neutrino emission from the core. Photon emission becomes the dominant cooling mechanism thereafter [Page *et al.* (2006)].

black hole. The other alternative is that the star explodes successfully as a supernova (i.e., the mantle collapses and accretion of matter becomes less important), giving birth to a hot PNS where neutrinos are trapped in the stellar core (stage "2" in Fig. 1.1). During the next stage of evolution, the star begins to rapidly lose neutrinos. This leads to a reduction of the pressure due to deleptonization, which would be followed by the formation of a black hole if the gravitational pull on the matter overcomes the pressure provided by the matter. If this does not happen, the star will continue to deleptonize itself as it is being heated-up by the Joule effect of the escaping neutrinos (stage "3" in Fig. 1.1). It is assumed that the maximum heating of the star occurs immediately after the neutrinos have left the star. Continued cooling via neutrino emission from the stellar core (stage "4" in

Fig. 1.1) [Malfatti (2020)] quickly reduces the star's temperature to just a few MeV or less [Page *et al.* (2006)]. At such temperatures the matter in the core can be described by a cold nuclear EOS and the corresponding star is referred to as a NS.

Understanding the physics behind a core collapse supernova and the subsequent formation of a PNS has been of interest in the particle and astrophysics communities for decades (see Mezzacappa (2005); Janka (2012); Burrows and Vartanyan (2021), and references therein). The well documented explosion of a type II supernova in the Large Magellanic Cloud in 1987 (SN1987a) was the first supernova event of this kind that could be studied in detail. Nineteen neutrinos have been detected from this event, which may be too few to provide a significant constraint on our understanding of the particle composition and physics of the supernova, but do provide an important milestone for these types of events. Since then, physicists have made great strides using numerical models to simulate supernova explosions (Camelio *et al.*, 2017). More difficult to describe through numerical codes is the lifespan of a PNS, but recent efforts as in (Hüdepohl *et al.*, 2010; Fischer *et al.*, 2010; Camelio *et al.*, 2017) have been able to more accurately describe the quasi-stationary evolution of a PNS.

In this book chapter we investigate the structure and composition of (hot) proto-neutron stars. In part one of the paper, we introduce the field-theoretic lagrangian that is used to compute models for the EOS of the matter in the cores of such stars. The relativistic mean field approach is used to describe the interactions among nucleons mediated by scalar, vector and iso-vector mesons. In our calculations, we focus on the density-dependent SWL, DD2, and GM1L nuclear models (Typel *et al.*, 2010; Spinella, 2017; Malfatti *et al.*, 2019; Spinella and Weber, 2020). All three models account for the presence of hyperons as well as of Δ baryons in hot and dense matter. The possible existence of deconfined quarks in such matter will be briefly discussed in this paper too. Investigations of this topic have also been carried out by (Steiner *et al.*, 2000; Shao, 2011; Mariani *et al.*, 2017; Malfatti *et al.*, 2019).

The relativistic finite-temperature Green function formalism is used to derive the equations that characterize ultra-hot and dense stellar matter (Weber, 1999). In part two of our study, the properties of non-rotating as well as rotating proto-neutron stars are studied by solving Einstein's field equation using the models for the EOS derived in part one of the paper. The rotating stellar models are computed fully self-consistently, as required by the general relativistic expression for the Kepler (mass shedding) frequency.

1.2   Modeling Hot and Dense Neutron Star Matter

1.2.1   *The Non-Linear Nuclear Lagrangian*

While a NS does get its namesake from the large quantities of neutrons created in the core during its birth, a more accurate depiction of interior composition a mixture of neutrons and protons whose electric charge is balanced by leptons ($L = e^-$, μ^-). Other particles may also exist in the core like hyperons ($B = [n,\ p,\ \Lambda,\ \Sigma^\pm,\ \Sigma^0,\ \Xi^0,\ \Xi^-]$ (Glendenning, 1985) and the electrically charged states of the Δ isobar (Pandharipande, 1971; Sawyer, 1972; Boguta, 1982). The existence of these particles is made possible only if their Fermi energies become large enough that existing baryon populations need to be rearranged so that a lower energy state can be reached (Glendenning, 1985). To understand how the baryons within the core interact, we shall make use of the non-linear density-dependent relativistic mean-field (DDRMF) theory. This theory describes the interactions between baryons in terms of meson exchange. These mesons include a scalar meson (σ) which describes attraction between baryons, a vector meson (ω) which describes repulsion, and an isovector meson (ρ) which is important to describe the baryon-baryon interactions in isospin asymmetric matter such as NS matter (Glendenning, 1985; Spinella, 2017). Due to the pion's odd parity, this particle does not contribute at the mean-field description of dense matter. The nuclear lagrangian of the theory is therefore given by (see also Weber (1999); Glendenning (2012); Spinella and Weber (2020); Sedrakian *et al.* (2022))

$$
\begin{aligned}
\mathcal{L} = {}& \sum_B \bar{\psi}_B \big[\gamma_\mu (i\partial^\mu - g_{\omega B}\omega^\mu - g_{\rho B}\boldsymbol{\tau}\cdot\boldsymbol{\rho}^\mu) - (m_B - g_{\sigma B}\sigma) \big]\psi_B \\
& + \frac{1}{2}(\partial_\mu\sigma\partial^\mu\sigma - m_\sigma^2\sigma^2) - \frac{1}{3}\tilde{b}_\sigma m_N (g_{\sigma N}\sigma)^3 - \frac{1}{4}\tilde{c}_\sigma (g_{\sigma N}\sigma)^4 \\
& - \frac{1}{4}\omega_{\mu\nu}\omega^{\mu\nu} + \frac{1}{2}m_\omega^2\omega_\mu\omega^\mu + \frac{1}{2}m_\rho^2\boldsymbol{\rho}_\mu\cdot\boldsymbol{\rho}^\mu - \frac{1}{4}\boldsymbol{\rho}_{\mu\nu}\cdot\boldsymbol{\rho}^{\mu\nu},
\end{aligned}
\tag{1.2}
$$

where ψ_B stands for the various baryon fields, $g_{\sigma B}$, $g_{\omega B}$ and $g_{\rho B}$ are (density dependent) meson-baryon coupling constants, and $\tilde{b}_\sigma$ and $\tilde{c}_\sigma$ denote two additional coupling parameters associated with non-linear (cubic and quartic) self-interactions introduced by Boguta and Bodmer (1977). The density dependent coupling constants are given by Typel (2018)

$$
g_{iB}(n) = g_{iB}(n_0)a_i \left[1 + b_i(n/n_0 + d_i)^2\right]\left[1 + c_i(n/n_0 + d_i)^2\right]^{-1}, \tag{1.3}
$$

for σ and ω mesons ($i = \sigma,\ \omega$), and by

$$
g_{\rho B}(n) = g_{\rho B}(n_0)\exp\left[-a_\rho\left(n/n_0 - 1\right)\right], \tag{1.4}
$$

for ρ mesons. Here the choice of parameters a_i, b_i, c_i, and d_i account for nuclear medium effects, and are fixed by the binding energies, charge, and diffraction radii, spin-orbit splittings, and the neutron skin thickness of finite nuclei.

The quantities m_B, m_σ, m_ω, m_ρ in Eq. (1.2) denote the masses of baryons and mesons and m_N is the nucleon mass. The quantity $\boldsymbol{\tau} = (\tau_1, \tau_2, \tau_3)$ are the Pauli isospin matrices. The quantities $\omega^{\mu\nu}$ and $\boldsymbol{\rho}^{\mu\nu}$ denote meson field tensors, where $\omega^{\mu\nu} = \partial^\mu\omega^\nu - \partial^\nu\omega^\mu$ and $\boldsymbol{\rho}^{\mu\nu} = \partial^\mu\boldsymbol{\rho}^\nu - \partial^\nu\boldsymbol{\rho}^\mu$. The field equations of the baryon and meson fields are obtained by evaluating the Euler-Lagrange equations for the fields in Eq. (1.2). This leads for the baryon fields to

$$\left(i\gamma^\mu\partial_\mu - m_B\right)\psi_B = \left(g_{\omega B}\gamma^\mu\omega_\mu + \tfrac{1}{2}g_{\rho B}\gamma^\mu\boldsymbol{\tau}\cdot\boldsymbol{\rho_\mu} - g_{\sigma B}\sigma\right)\psi_B\,. \qquad (1.5)$$

The field equation of the scalar σ-meson is given by

$$\left(\partial^\mu\partial_\mu + m_\sigma^2\right)\sigma = \sum_B g_{\sigma B}\bar{\psi}_B\psi_B - b_\sigma m_n g_{\sigma N}\left(g_{\sigma N}\sigma\right)^2 - c_\sigma g_{\sigma N}\left(g_{\sigma N}\sigma\right)^3\,,$$
$$\qquad (1.6)$$

and the field equations of the vector mesons have the form

$$\partial^\mu\omega_{\mu\nu} + m_\omega^2\omega_\nu = \sum_B g_{\omega B}\bar{\psi}_B\gamma_\nu\psi_B\,, \qquad (1.7)$$

$$\partial^\mu\boldsymbol{\rho}_{\mu\nu} + m_\rho^2\boldsymbol{\rho}_\nu = \sum_B g_{\rho B}\bar{\psi}_B\boldsymbol{\tau}\gamma_\nu\psi_B\,. \qquad (1.8)$$

In relativistic mean-field approximation, the field equations (1.5) through (1.8) become

$$m_\sigma^2\bar{\sigma} = \sum_B g_{\sigma B}n_B^s - \tilde{b}_\sigma\,m_N\,g_{\sigma N}(g_{\sigma N}\bar{\sigma})^2 - \tilde{c}_\sigma\,g_{\sigma N}\left(g_{\sigma N}\bar{\sigma}\right)^3\,, \qquad (1.9)$$

$$m_\omega^2\bar{\omega} = \sum_B g_{\omega B}n_B\,, \qquad (1.10)$$

$$m_\rho^2\bar{\rho} = \sum_B g_{\rho B}I_{3B}n_B\,, \qquad (1.11)$$

where I_{3B} is the 3-component of isospin and n_B^s and n_B are the scalar and particle number densities for each baryon B. The latter are given by

$$n_B = \langle\psi_B^\dagger(x)\,\psi_B(x)\rangle\,, \qquad (1.12)$$

$$n_B^s = \langle\bar{\psi}_B(x)\,\psi_B(x)\rangle\,, \qquad (1.13)$$

respectively, where $\psi_B^\dagger$ denotes the conjugate Dirac spinor and $\bar{\psi} \equiv \psi_B^\dagger\gamma^0$ stands for the adjoint Dirac spinor. To keep the notation to a minimum, we use the definition $x \equiv (x^0, \boldsymbol{x})$.

1.2.2 *Baryonic Field Theory at Finite Density and Temperature*

To calculate the densities (1.12) and (1.13) for NS matter at finite temperature, we use the finite-temperature Green function formalism. The starting point is the spectral function representation of the two-point Green function given by (Dolan and Jackiw, 1974; Weber, 1999)

$$g^B(p^0, \boldsymbol{p}) = \int d\omega \, \frac{a^B(\omega, \boldsymbol{p})}{\omega - (p^0 - \mu_B)(1 + i\eta)} \tag{1.14}$$
$$-2i\pi \, \text{sign}(p^0 - \mu_B) \, \frac{1}{\exp(|p^0 - \mu_B|/T) + 1} \, a^B(p^0 - \mu_B, \boldsymbol{p}) \,,$$

where μ_B denotes the chemical potential of a baryon of type B and a^B stands for the spectral function of that baryon ($\eta > 0$ and infinitesimally small). The spin and isospin dependences of g^B and a^B are not shown explicitly. The spectral function is obtained by evaluating

$$a^B(\omega, \boldsymbol{p}) = \frac{1}{2i\pi} \left(\tilde{g}^B(\omega + i\eta, \boldsymbol{p}) - \tilde{g}^B(\omega - i\eta, \boldsymbol{p}) \right) . \tag{1.15}$$

Here $\tilde{g}^B$ denotes the analytically continued two-point Green function, which obeys the analytically continued Dyson equation,

$$\left(\gamma^0(z + \mu_B) - \boldsymbol{\gamma} \cdot \boldsymbol{p} - m_B - \tilde{\Sigma}^B(z, \boldsymbol{p}) \right) \tilde{g}^B(z, \boldsymbol{p}) = -1 \,. \tag{1.16}$$

The spectral function has a scalar, vector and a time-like contribution generally written as (Weber, 1999)

$$a^B(\boldsymbol{p}) = a_S^B(\boldsymbol{p}) + \boldsymbol{\gamma} \cdot \hat{\boldsymbol{p}} \, a_V^B(\boldsymbol{p}) + \gamma^0 a_0^B(\boldsymbol{p}) \,, \tag{1.17}$$

where $a_S^B(\boldsymbol{p}) = m_B^*/(2E_B^*(\boldsymbol{p}))$, $a_V^B(\boldsymbol{p}) = -|\boldsymbol{p}|/(2E_B^*(\boldsymbol{p}))$, and $a_0^B(\boldsymbol{p}) = 1/2$. For thermally excited anti-baryon states one has

$$\bar{a}^B(\boldsymbol{p}) = \bar{a}_S^B(\boldsymbol{p}) + \boldsymbol{\gamma} \cdot \hat{\boldsymbol{p}} \, \bar{a}_V^B(\boldsymbol{p}) + \gamma^0 \bar{a}_0^B(\boldsymbol{p}) \,, \tag{1.18}$$

where $\bar{a}_S^B(\boldsymbol{p}) = -m_B^*/(2E_B^*(\boldsymbol{p}))$, $\bar{a}_V^B(\boldsymbol{p}) = |\boldsymbol{p}|/(2E_B^*(\boldsymbol{p}))$, and $a_0^B(\boldsymbol{p}) = 1/2$. The effective single-baryon energy, E_B^* and effective baryon mass, m_B^*, are given by

$$E_B^*(\boldsymbol{p}) = \sqrt{\boldsymbol{p}^2 + m_B^{*\,2}} \tag{1.19}$$

and

$$m_B^* = m_B - g_{\sigma B} \bar{\sigma} \,, \tag{1.20}$$

respectively.

In terms of the two-point Green function, the expression for the baryon number density (1.12) becomes

$$n_B = i \operatorname{Tr} \gamma^0 \int d^3 \boldsymbol{x} \left(g^B(x, x^+) + g^B(x, x^-) \right) , \qquad (1.21)$$

where $x^\pm = (x^0 \pm \eta, \boldsymbol{x})$. The trace is to be taken over the spin and isospin matrix indices. Transformation of Eq. (1.21) to momentum space leads to

$$n_B = i \operatorname{Tr} \gamma^0 \int \frac{d^4 p}{(2\pi)^4} \left(e^{i\eta p^0} + e^{-i\eta p^0} \right) g^B(p) . \qquad (1.22)$$

Next we note that

$$\int \frac{d^4 p}{(2\pi)^4} e^{i\eta p^0} p^0 g^B(p^0, \boldsymbol{p}) = -i \int \frac{d^3 \boldsymbol{p}}{(2\pi)^3} a^B(\boldsymbol{p}) \omega_B(\boldsymbol{p}) f_{B^-}(\boldsymbol{p}) , \quad (1.23)$$

and

$$\int \frac{d^4 p}{(2\pi)^4} e^{-i\eta p^0} p^0 g^B(p^0, \boldsymbol{p}) = i \int \frac{d^3 \boldsymbol{p}}{(2\pi)^3} \bar{a}^B(\boldsymbol{p}) \bar{\omega}_B(\boldsymbol{p}) f_{B^+}(\boldsymbol{p}) , \quad (1.24)$$

which leads for Eq. (1.22) to

$$n_B = \gamma_B \int \frac{d^3 \boldsymbol{p}}{(2\pi)^3} \left(f_{B^-}(\boldsymbol{p}) - f_{B^+}(\boldsymbol{p}) \right) , \qquad (1.25)$$

where $\gamma_B \equiv (2J_B + 1)$ accounts for the spin-degeneracy. The quantities $f_{B^\pm}$ in Eq. (1.25) denote Fermi-Dirac distribution functions given by

$$f_{B^-}(\boldsymbol{p}) = \frac{1}{e^{(E_B^*(\boldsymbol{p}) - \mu_B^*)/T} + 1} , \qquad (1.26)$$

and

$$f_{B^+}(\boldsymbol{p}) = \frac{1}{e^{(-\bar{E}_B^*(\boldsymbol{p}) + \mu_B^*)/T} + 1} . \qquad (1.27)$$

The quantity μ_B^* in Eqs. (1.26) and (1.27), given by

$$\mu_B^* = \mu_B - g_{\omega B} \bar{\omega} - g_{\rho B} \bar{\rho} I_{3B} - \tilde{R} , \qquad (1.28)$$

defines the effective baryon chemical potential in terms of the standard chemical potential and the mean-fields of σ and ρ mesons. The quantity $\tilde{R}$ is the rearrangement term given by (Fuchs *et al.*, 1995; Spinella and Weber, 2020)

$$\tilde{R} = \sum_B \left(\frac{\partial g_{\omega B}(n)}{\partial n} n_B \bar{\omega} + \frac{\partial g_{\rho B}(n)}{\partial n} I_{3B} n_B \bar{\rho} \frac{\partial g_{\sigma B}(n)}{\partial n} n_B^s \bar{\sigma} \right) . \quad (1.29)$$

This term is mandatory for thermodynamic consistency, proven with the Hugenholtz-van Hove theorem that relates the total baryonic pressure

(which contains the rearrangement term) of a particle to its chemical potential (Hofmann *et al.*, 2001). The expression of the total baryonic pressure of the standard non-linear relativistic mean-field theory therefore contains the additional term $n\tilde{R}$ (see Eq. (1.54)).

The single-baryon energies, $\omega_B(\boldsymbol{p})$, are given in terms of these meson fields plus the effective single-baryon energies, E_B^*, according to the relation

$$\omega_B(\boldsymbol{p}) = g_{\omega B}\bar{\omega} + g_{\rho B}I_{3B}\bar{\rho} + E_B^*(\boldsymbol{p}) . \tag{1.30}$$

Similarly, the single-particle energies of thermally excited anti-baryon states, $\bar{\omega}_B(\boldsymbol{p})$, are given by

$$\bar{\omega}_B(\boldsymbol{p}) = g_{\omega B}\bar{\omega} + g_{\rho B}I_{3B}\bar{\rho} - E_B^*(\boldsymbol{p}) . \tag{1.31}$$

From the above relations, one sees that for baryons

$$\omega_B(\boldsymbol{p}) - \mu_B = E_B^*(\boldsymbol{p}) - \mu_B^* , \tag{1.32}$$

and for states outside the Fermi sea of anti-particles

$$- \bar{\omega}_B(\boldsymbol{p}) + \mu_B = E_B^*(\boldsymbol{p}) + \mu_B^* . \tag{1.33}$$

With these definitions, the traces in Eq. (1.22) and in the expressions for the energy density and pressure to be discussed below can be calculated. In particular, one obtains

$$\mathrm{Tr}\, a^B = \gamma_B m_B^*/E_B^* , \quad \mathrm{Tr}\, \bar{a}^B = -\gamma_B m_B^*/E_B^* , \tag{1.34}$$

$$\mathrm{Tr}\, \gamma^0 a^B = \gamma_B , \quad \mathrm{Tr}\, \gamma^0 \bar{a}^B = -\gamma_B . \tag{1.35}$$

Next we turn to the scalar density, n_B^s, defined in Eq. (1.13). Expressed in terms of the two-point Green function, Eq. (1.13) reads

$$n_B^s = i\,\mathrm{Tr}\int d^3\boldsymbol{x}\,\left(g^B(x,x^+) + g^B(x,x^-)\right) . \tag{1.36}$$

Transforming this expression to momentum space gives

$$n_B^s = i\,\mathrm{Tr}\int \frac{d^4p}{(2\pi)^4}\,\left(\mathrm{e}^{i\eta p^0} + \mathrm{e}^{-i\eta p^0}\right) g^B(p) . \tag{1.37}$$

By making use of Eq. (1.24), the integration of p^0 can be carried out analytically. The Green functions then get replaced by the baryon spectral functions and the Fermi-Dirac distribution functions, leading to the final result for the scalar density given by

$$n_B^s = \gamma_B \int \frac{d^3\boldsymbol{p}}{(2\pi)^3} \frac{m_B^*}{E_B^*(\boldsymbol{p})}\,(f_{B^-}(\boldsymbol{p}) - f_{B^+}(\boldsymbol{p})) . \tag{1.38}$$

1.3   Composition and EOS of Hot and Dense (Proto-) Neutron Star Matter

The total energy density and pressure of the stellar matter are calculated from the energy-momentum tensor

$$T_{\mu\nu}(x) = g_{\mu\nu}\,\mathcal{L}(x) + \sum_B \frac{\partial \mathcal{L}(x)}{\partial\,\partial^\mu\psi_B(x)}\,\partial_\nu\psi_B(x)\,, \tag{1.39}$$

with the lagrangian $\mathcal{L}$ given by Eq. (1.2). The energy density and pressure are given by $\epsilon = \langle T^{00}\rangle$ and $P = \frac{1}{3}\sum_k \langle T^{kk}\rangle$, respectively. Using the Green function formalism, the expression for the energy density is given by (Weber, 1999)

$$\begin{aligned}
\epsilon = \ & i\sum_B \mathrm{Tr}\int \frac{d^4p}{(2\pi)^4}\left(\mathrm{e}^{i\eta p^0} + \mathrm{e}^{-i\eta p^0}\right) \\
& \times \left(p^0\gamma^0 - \frac{1}{2}\left(g_{\sigma B}\bar\sigma + \gamma^0\left(g_{\omega B}\bar\omega + g_{\rho B}I_{3B}\bar\rho\right)\right)\right)g^B(p) \\
& -\frac{1}{6}\tilde{b}_\sigma m_N\left(g_{\sigma N}\sigma\right)^3 - \frac{1}{4}\tilde{c}_\sigma\left(g_{\sigma N}\sigma\right)^4\,.
\end{aligned} \tag{1.40}$$

The integration over p^0 in Eq. (1.40) can be carried out analytically via contour integration, which leads to

$$\int \frac{d^4p}{(2\pi)^4}\,\mathrm{e}^{i\eta p^0}g^B(p^0,\boldsymbol{p}) = -i\int \frac{d^3\boldsymbol{p}}{(2\pi)^3}\,a^B(\boldsymbol{p})f_{B-}(\boldsymbol{p}) \tag{1.41}$$

and

$$\int \frac{d^4p}{(2\pi)^4}\,\mathrm{e}^{-i\eta p^0}g^B(p^0,\boldsymbol{p}) = i\int \frac{d^3\boldsymbol{p}}{(2\pi)^3}\,\bar{a}^B(\boldsymbol{p})f_{B+}(\boldsymbol{p})\,. \tag{1.42}$$

The energy density is then given as a momentum integral over single-baryon energies, baryon spectral functions, and Fermi-Dirac distribution functions, as shown below:

$$\begin{aligned}
\epsilon = \ & \sum_B \mathrm{Tr}\int \frac{d^3\boldsymbol{p}}{(2\pi)^3}\left(\omega^B(\boldsymbol{p})\gamma^0 a^B(\boldsymbol{p})f_{B-}(\boldsymbol{p}) - \bar\omega^B(\boldsymbol{p})\gamma^0\bar{a}^B(\boldsymbol{p})f_{B+}(\boldsymbol{p})\right) \\
& -\frac{1}{2}\sum_B \mathrm{Tr}\int \frac{d^3\boldsymbol{p}}{(2\pi)^3}\left(\left(-g_{\sigma B}\bar\sigma + \gamma^0\left(g_{\omega B}\bar\omega + g_{\rho B}I_{3B}\bar\rho\right)\right)a^B(\boldsymbol{p})f_{B-}(\boldsymbol{p})\right. \\
& \left. \qquad\qquad - \left(-g_{\sigma B}\bar\sigma + \gamma^0\left(g_{\omega B}\bar\omega + g_{\rho B}I_{3B}\bar\rho\right)\right)\bar{a}^B(\boldsymbol{p})f_{B+}(\boldsymbol{p})\right) \\
& -\frac{1}{6}\tilde{b}_\sigma m_N\left(g_{\sigma N}\sigma\right)^3 - \frac{1}{4}\tilde{c}_\sigma\left(g_{\sigma N}\sigma\right)^4\,.
\end{aligned} \tag{1.43}$$

By making use of Eqs. (1.31), (1.34) and (1.35), this expression can be written as

$$
\begin{aligned}
\epsilon = &\sum_B \gamma_B \int \frac{d^3\boldsymbol{p}}{(2\pi)^3}\, E_B^*(\boldsymbol{p})\,(f_{B-}(\boldsymbol{p}) + f_{B+}(\boldsymbol{p})) \\
&+ \sum_B \gamma_B \int \frac{d^3\boldsymbol{p}}{(2\pi)^3}\,(g_{\omega B}\bar{\omega} + g_{\rho B} I_{3B}\bar{\rho})\,(f_{B-}(\boldsymbol{p}) - f_{B+}(\boldsymbol{p})) \\
&- \frac{1}{2}\sum_B \gamma_B \int \frac{d^3\boldsymbol{p}}{(2\pi)^3}\left(-\frac{m_B^*}{E_B^*(\mathbf{p})}g_{\sigma B}\bar{\sigma} + \gamma^0\,(g_{\omega B}\bar{\omega} + g_{\rho B} I_{3B}\bar{\rho})\right) \\
&\hspace{4cm}\times (f_{B-}(\boldsymbol{p}) - f_{B+}(\boldsymbol{p})) \\
&- \frac{1}{6}\tilde{b}_\sigma m_N (g_{\sigma N}\sigma)^3 - \frac{1}{4}\tilde{c}_\sigma (g_{\sigma N}\sigma)^4 .
\end{aligned}
\tag{1.44}
$$

It is customary to express Eq. (1.44) in a more compact way. This is accomplished by noticing that, according to Eq. (1.38), the integral over the first term in the third line above can be written as

$$
\sum_B \gamma_B \int \frac{d^3\boldsymbol{p}}{(2\pi)^3}\,\frac{m_B^*}{E_B^*(\mathbf{p})}g_{\sigma B}\bar{\sigma}\,(f_{B-}(\boldsymbol{p}) + f_{B+}(\boldsymbol{p})) = \sum_B g_{\sigma B} n_B^s \bar{\sigma}. \tag{1.45}
$$

Making use of the σ-meson field equation (1.9) to replace $\sum_B g_{\sigma B} n_B^s$ in Eq. (1.45) leads after some algebra to the final result for the energy density given by (Weber, 1999)

$$
\begin{aligned}
\epsilon = &\sum_B \gamma_B \int \frac{d^3\boldsymbol{p}}{(2\pi)^3}\, E_B^*(\boldsymbol{p})\,(f_{B-}(\boldsymbol{p}) + f_{B+}(\boldsymbol{p})) + \frac{1}{2}m_\sigma^2 \bar{\sigma}^2 + \frac{1}{2}m_\omega^2 \bar{\omega}^2 \\
&+ \frac{1}{2}m_\rho^2 \bar{\rho}^2 + \frac{1}{3}\tilde{b}_\sigma m_N (g_{\sigma N}\sigma)^3 + \frac{1}{4}\tilde{c}_\sigma (g_{\sigma N}\sigma)^4 .
\end{aligned}
\tag{1.46}
$$

The expression for the pressure of hot NS matter has the form (Weber, 1999)

$$
\begin{aligned}
P = \ &i\sum_B \mathrm{Tr} \int \frac{d^4 p}{(2\pi)^4}\left(e^{i\eta p^0} + e^{-i\eta p^0}\right) \\
&\hspace{1cm}\times \left(\frac{1}{3}\boldsymbol{\gamma}\cdot\hat{\boldsymbol{p}} + \frac{1}{2}\left(-g_{\sigma B}\bar{\sigma} + \gamma^0\,(g_{\omega B}\bar{\omega} + g_{\rho B} I_{3B}\bar{\rho})\right)\right)g^B(p) \\
&+ \frac{1}{6}\tilde{b}_\sigma m_N (g_{\sigma N}\sigma)^3 + \frac{1}{4}\tilde{c}_\sigma (g_{\sigma N}\sigma)^4 .
\end{aligned}
\tag{1.47}
$$

As for the energy density, the integration of p^0 can be carried out analytically using the mathematical relations shown in Eqs. (1.41) and (1.42).

This leads to

$$P = \frac{1}{3} \sum_B \mathrm{Tr} \int \frac{d^3\boldsymbol{p}}{(2\pi)^3} \left(\boldsymbol{\gamma} \cdot \hat{\boldsymbol{p}} \, a^B(\boldsymbol{p}) f_{B^-}(\boldsymbol{p}) - \boldsymbol{\gamma} \cdot \hat{\boldsymbol{p}} \, \bar{a}^B(\boldsymbol{p}) f_{B^+}(\boldsymbol{p}) \right)$$

$$+ \frac{1}{2} \sum_B \mathrm{Tr} \int \frac{d^3\boldsymbol{p}}{(2\pi)^3} \left(\left(-g_{\sigma B}\bar{\sigma} + \gamma^0 \left(g_{\omega B}\bar{\omega} + g_{\rho B} I_{3B}\bar{\rho} \right) \right) a^B(\boldsymbol{p}) f_{B^-}(\boldsymbol{p}) \right.$$

$$\left. - \left(-g_{\sigma B}\bar{\sigma} + \gamma^0 \left(g_{\omega B}\bar{\omega} + g_{\rho B} I_{3B}\bar{\rho} \right) \right) \bar{a}^B(\boldsymbol{p}) f_{B^+}(\boldsymbol{p}) \right)$$

$$+ \frac{1}{6}\tilde{b}_\sigma m_N \left(g_{\sigma N}\sigma \right)^3 + \frac{1}{4}\tilde{c}_\sigma \left(g_{\sigma N}\sigma \right)^4 . \tag{1.48}$$

With the help of Eqs. (1.17) and (1.18) for the spectral functions and Eqs. (1.34) and (1.35) for the traces, expression Eq. (1.48) can be written as

$$P = \frac{1}{3} \sum_B \gamma_B \int \frac{d^3\boldsymbol{p}}{(2\pi)^3} \frac{\boldsymbol{p}^2}{E_B^*(\boldsymbol{p})} \left(f_{B^-}(\boldsymbol{p}) + f_{B^+}(\boldsymbol{p}) \right)$$

$$+ \frac{1}{2} \sum_B \gamma_B \int \frac{d^3\boldsymbol{p}}{(2\pi)^3} \left(-\frac{m_B^*}{E_B^*(\boldsymbol{p})} g_{\sigma B}\bar{\sigma} + g_{\omega B}\bar{\omega} + g_{\rho B} I_{3B}\bar{\rho} \right)$$

$$\times \left(f_{B^-}(\boldsymbol{p}) - f_{B^+}(\boldsymbol{p}) \right)$$

$$+ \frac{1}{6}\tilde{b}_\sigma m_N \left(g_{\sigma N}\sigma \right)^3 + \frac{1}{4}\tilde{c}_\sigma \left(g_{\sigma N}\sigma \right)^4 . \tag{1.49}$$

The second line in this equation can be written in terms of the scalar and baryon number densities. To see this we begin with Eq. (1.38), from which it follows that

$$\sum_B \gamma_B \int \frac{d^3\boldsymbol{p}}{(2\pi)^3} \frac{m_B^*}{E_B^*(\boldsymbol{p})} g_{\sigma B}\bar{\sigma} \left(f_{B^-}(\boldsymbol{p}) - f_{B^+}(\boldsymbol{p}) \right) = \sum_B g_{\sigma B} n_B^s \bar{\sigma} . \tag{1.50}$$

On the other hand, it is known from the σ-meson field equation (1.9) that

$$\sum_B g_{\sigma B} n_B^s \bar{\sigma} = m_\sigma^2 \bar{\sigma}^2 + \tilde{b}_\sigma m_N \left(g_{\sigma N}\sigma \right)^3 + \tilde{c}_\sigma \left(g_{\sigma N}\sigma \right)^4 . \tag{1.51}$$

Similarly, for the ω-meson dependent term in Eq. (1.49) we have

$$\sum_B \gamma_B \int \frac{d^3\boldsymbol{p}}{(2\pi)^3} g_{\omega B}\bar{\omega} \left(f_{B^-}(\boldsymbol{p}) - f_{B^+}(\boldsymbol{p}) \right) = \sum_B g_{\omega B} n_B \bar{\omega} ,$$

$$= m_\omega^2 \bar{\omega}^2 , \tag{1.52}$$

and for the ρ-meson dependent term

$$\sum_B \gamma_B \int \frac{d^3\boldsymbol{p}}{(2\pi)^3} g_{\rho B} I_{3B}\bar{\rho} \left(f_{B^-}(\boldsymbol{p}) - f_{B^+}(\boldsymbol{p}) \right) = \sum_B g_{\rho B} I_{3B} n^B \bar{\rho} ,$$

$$= m_\rho^2 \bar{\rho}^2 \tag{1.53}$$

Substituting Eqs. (1.50) through (1.53) into Eq. (1.49) leads for the pressure of NS matter to (Weber, 1999)

$$
P = \frac{1}{3} \sum_B \gamma_B \int \frac{d^3\boldsymbol{p}}{(2\pi)^3} \frac{\boldsymbol{p}^2}{E_B^*(\boldsymbol{p})} \left(f_{B^-}(\boldsymbol{p}) + f_{B^+}(\boldsymbol{p}) \right) - \frac{1}{2} m_\sigma^2 \bar{\sigma}^2 + \frac{1}{2} m_\omega^2 \bar{\omega}^2
$$
$$
+ \frac{1}{2} m_\rho^2 \bar{\rho}^2 - \frac{1}{3} \tilde{b}_\sigma m_N \left(g_{\sigma N} \sigma \right)^3 - \frac{1}{4} \tilde{c}_\sigma \left(g_{\sigma N} \sigma \right)^4 + n \tilde{R} \,. \qquad (1.54)
$$

1.3.1 *Leptons and Neutrinos*

Leptons are treated as free Fermi gases with the grand canonical potential given by (Weber, 1999; Malfatti *et al.*, 2019)

$$
\Omega_L = -\sum_L \frac{\gamma_L}{3} \int \frac{d^3\boldsymbol{p}}{(2\pi)^3} \frac{\boldsymbol{p}^2}{E_L(\boldsymbol{p})} \left(f_{L^-}(p) + f_{L^+}(p) \right) \,, \qquad (1.55)
$$

where $\gamma_L = (2J_L + 1)$ is the lepton degeneracy factor. The sum over L in Eq. (1.55) runs over e^- and μ^-, with masses m_L, and massless neutrinos, ν_e, in the case they are trapped in a PNS (see 1.3.2, 1.3.3). The lepton distribution function is given by

$$
f_{L^\mp}(p) = \frac{1}{e^{(E_L(p)\mp\mu_L)/T} + 1} \,, \qquad (1.56)
$$

where $E_L(p) = \sqrt{p^2 + m_L^2}$ denotes the energy-momentum relation of free leptons.

1.3.2 *Chemical Equilibrium and Electric Charge Neutrality*

Three important constraints must be taken into account when determining the EOS of PNS matter: electric charge neutrality, baryon number conservation, and chemical equilibrium. Neutron star matter must be charge neutral, satisfying (Glendenning, 1985; Weber, 1999; Malfatti *et al.*, 2019)

$$
\sum_B q_B \, n_B + \sum_L q_L \, n_L = 0 \,, \qquad (1.57)
$$

where q_B and q_L are baryon and lepton electric charge, respectively. Baryon number must also be conserved, which leads to

$$
\sum_B n_B - n = 0 \,, \qquad (1.58)
$$

Finally, the constraint of chemical equilibrium for hadronic matter can be defined as (Prakash *et al.*, 1997)

$$
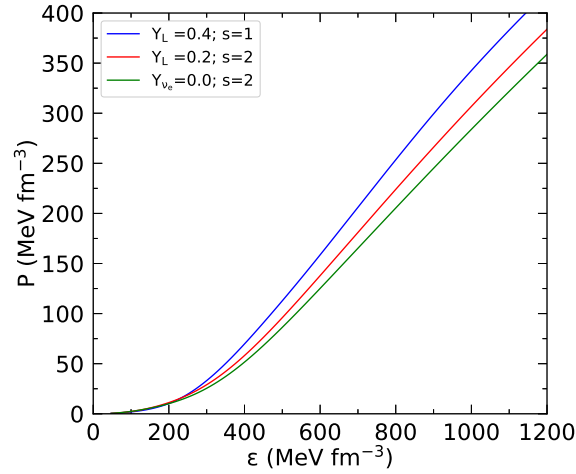\mu_B = \mu_n + q_B (\mu_e - \mu_{\nu_e}) \,, \qquad (1.59)
$$

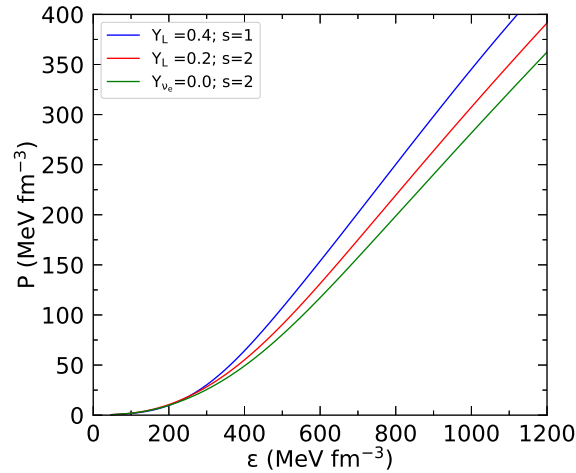Fig. 1.2   Pressure as a function of energy density for the DD2 parameter set.

Fig. 1.3   Pressure as a function of energy density for the GM1L parameter set.

where μ_n, μ_e and μ_{ν_e} are the neutron, electron and neutrino chemical potentials, respectively. The chemical potential of the latter follows from the equilibrium reaction

$$e^- \leftrightarrow \mu^- + \nu_e + \bar{\nu}_\mu \,, \tag{1.60}$$

which leads for the corresponding chemical potentials to the condition

$$\mu_e = \mu_\mu + \mu_{\nu_e} + \mu_{\bar{\nu}_\mu} \,. \tag{1.61}$$
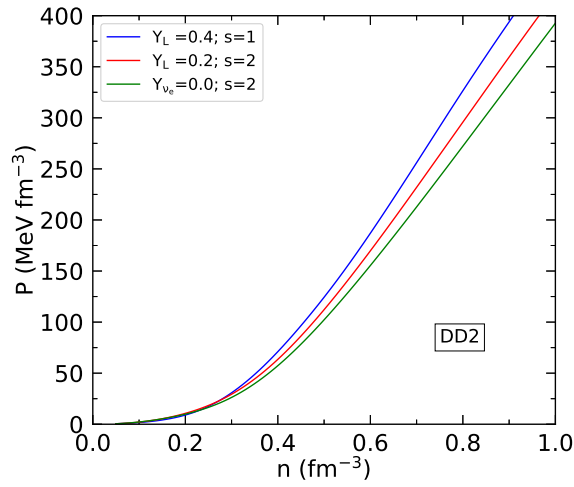
Fig. 1.4   Pressure as a function of baryon number density for the DD2 parameter set.
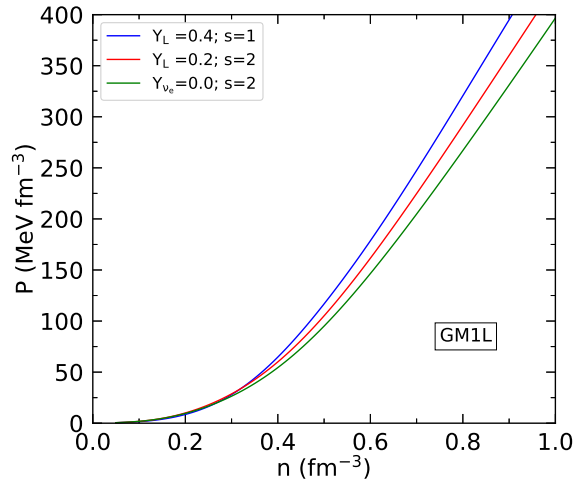
Fig. 1.5   Same as Fig. 1.4, but for the GM1L parameter set.

Neutrinos are trapped inside of a proto-neutron star immediately after its formation. Mathematically this is expressed as (Prakash *et al.*, 1997; Mal-

fatti *et al.*, 2019)

$$Y_{L_e} = \frac{n_e + n_{\nu_e}}{n} \,, \tag{1.62}$$

$$Y_{L_\mu} = \frac{n_\mu + n_{\nu_\mu}}{n} = 0 \,, \tag{1.63}$$

where n_e, n_μ, n_{ν_e}, and n_{ν_μ} denote the number densities of electrons, muons, electron neutrinos, and muon neutrinos, respectively. During this very early stellar phase, the matter is opaque to neutrinos and the composition of the matter is characterized by three independent chemical potentials, namely μ_n, μ_e, and μ_{ν_e}. The condition $Y_{L_\mu} = 0$ expressed in Eq. (1.63) reflects the fact that only very few muons are present in PNS matter right after core bounce, when neutrinos are still trapped. The value of Y_{L_e} ($\lesssim 0.4$) depends on the efficiency of electron capture reactions during the initial state of the formation of proto-neutron stars (Prakash *et al.*, 1997). The quantity Y_L, defined as

$$Y_L = Y_e + Y_{\nu_e} \,, \tag{1.64}$$

is used in the figures to show the relative fractions of electrons and neutrinos for which the respective curves have been computed.

In Figs. 1.2 and 1.3 we show how pressure varies as a function of energy density for the DD2 and GM1L parameter sets. Figures 1.4 and 1.5 show the pressure as a function baryon number density for DD2 and GM1L. Details of these parameter sets including the coupling values used to compute the DD2 and GM1L EOSs will be discussed in Sec. 1.5. The EOSs are shown for different lepton fractions, Y_L, and entropies (per baryon), s which correspond to the main characteristic stages in the life of a proto-neutron star (briefly summarized at the beginning of Sec. 1.3.3). The EOSs (as well as all other dense-matter properties presented in this chapter) shown in Figs. 1.2 and 1.3 have been computed for $B = n, p, \Lambda, \Sigma^\pm, \Sigma^0, \Xi^0, \Xi^-$, all electrically charged states of the $\Delta(1232)$ baryon, and $L = e, \mu, \nu_e$.

The values of the baryon–hyperon coupling constants will be discussed in detail in Sec. 1.5.1. The values chosen for the Δ–hyperon couplings are $x_{\sigma\Delta} = x_{\omega\Delta} = 1.1$ and $x_{\rho\Delta} = 1.0$ as described in Sec. 1.5.2. A general investigation of the $\Delta(1232)$ coupling spaces is provided in Sec. 1.5.3.

1.3.3   *Composition of Hot and Dense Matter*

In this section we show the composition of hot and dense matter as it exists in the cores of proto-neutron stars. Following the core bounce post
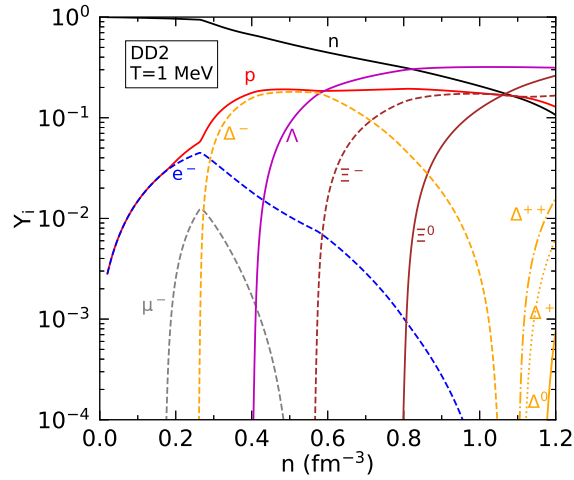
Fig. 1.6   Composition of dense stellar matter computed for DD2 parametrization and a temperature of $T = 1$ MeV.
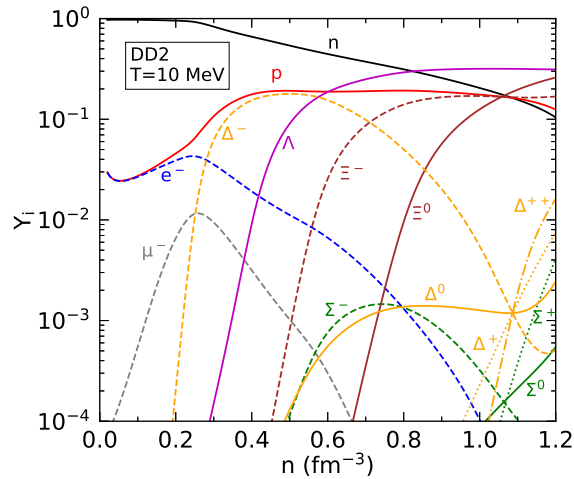

Fig. 1.7   Same as Fig. 1.6, but for a stellar temperature of $T = 10$ MeV.

supernova explosion, PNSs experience a deleptonization stage where hot, lepton-rich matter becomes lepton-poor over the course of about a minute. During this time, the entropy per baryon and lepton fraction of the dense matter within the PNS core change quickly. These values start at around $s = 1$ and $Y_L = 0.4$, change to $s = 2$ and $Y_L = 0.2$ after around 0.5 to 1

Contents   21
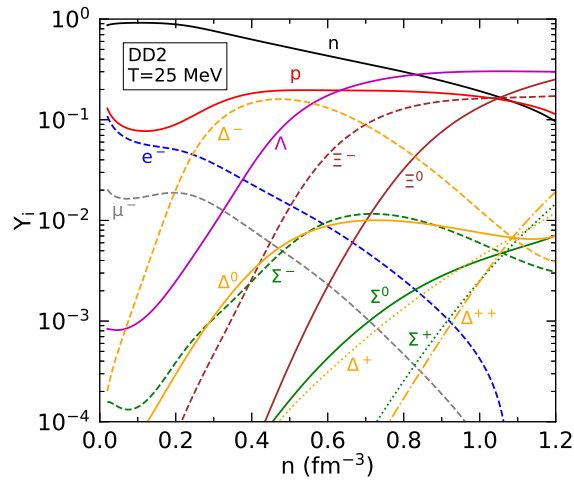

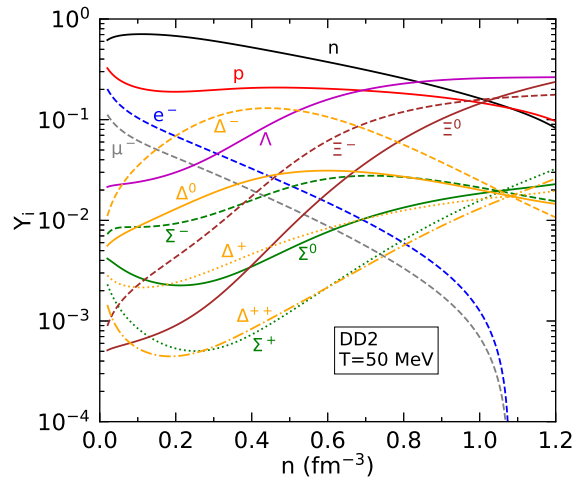Fig. 1.8   Same as Fig. 1.6, but for a stellar temperature of $T = 25$ MeV.

Fig. 1.9   Same as Fig. 1.6, but for a stellar temperature of $T = 50$ MeV.

seconds, and take values of $s = 2$ and $Y_{\nu_e} = 0$ about 15 to 30 seconds after the birth of a proto-neutron star (Prakash *et al.*, 1997; Strobel *et al.*, 1999; Malfatti *et al.*, 2019). As neutrinos and photons diffuse from the object the stellar temperature drops to less than 1 MeV and a hot PNS becomes a cold NS.
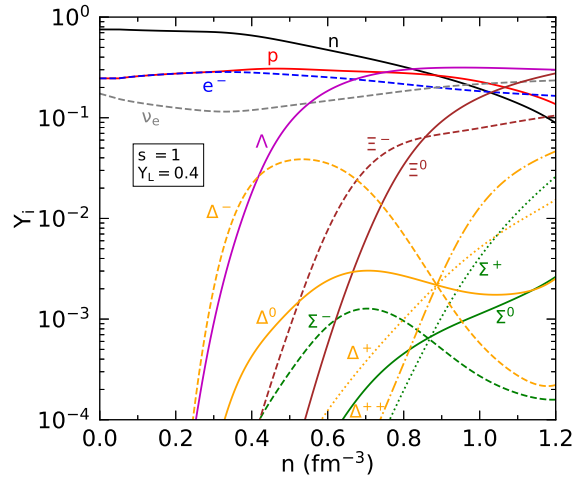
Fig. 1.10   Baryon-lepton composition of PNS matter obtained for DD2 model with $s = 1$ and $Y_L = 0.4$ (Malfatti *et al.*, 2019).
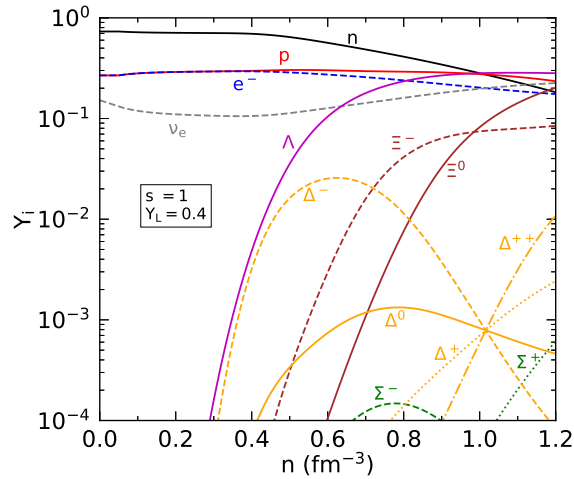

Fig. 1.11   Baryon-lepton composition of PNS matter obtained for GM1L model with $s = 1$ and $Y_L = 0.4$ (Malfatti *et al.*, 2019).

Figures 1.6 through 1.9 illustrate how drastically the particle composition in the core of a neutron star changes with temperature. In fact, as can be seen by comparing the compositions shown in Figs. 1.6 and 1.8 with each other, the particle composition at a temperature of 25 MeV no longer
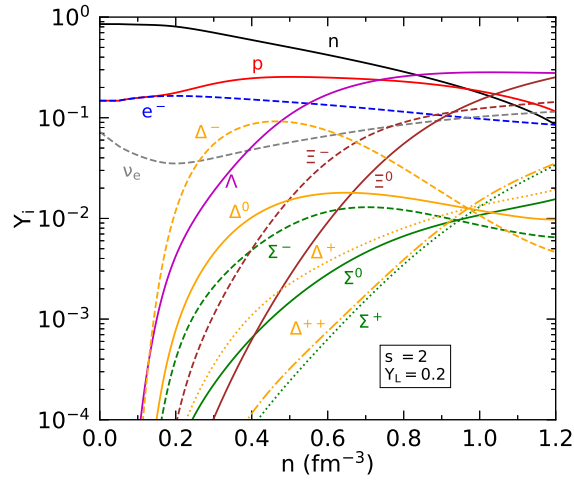
Fig. 1.12   Baryon-lepton composition of PNS matter obtained for DD2 model with $s = 2$ and $Y_L = 0.2$ (Malfatti *et al.*, 2019).
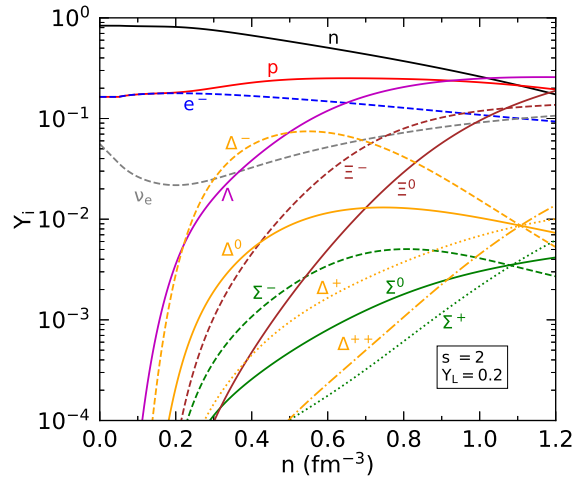

Fig. 1.13   Baryon-lepton composition of PNS matter obtained for GM1L model with $s = 2$ and $Y_L = 0.2$ (Malfatti *et al.*, 2019).

resembles the zero-temperature (i.e., 1 MeV) composition at all. Moreover, in matter at even higher temperatures the threshold densities of all the baryons have changed so much that all baryonic particle states taken into account in our calculations are present at all densities, as shown in Fig. 1.9.
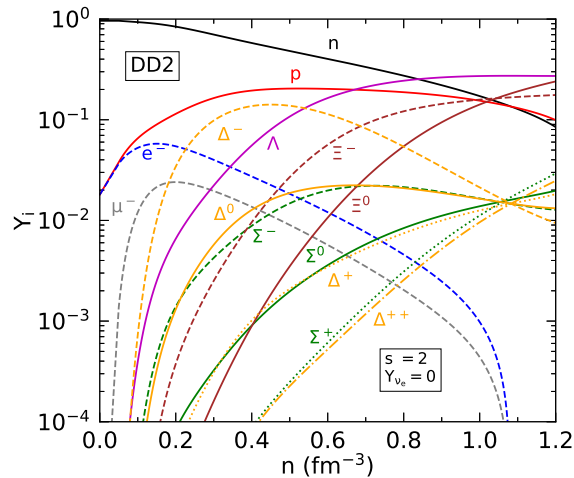
Fig. 1.14   Baryon-lepton composition of PNS matter obtained for DD2 model with $s = 2$ and $Y_{\nu_e} = 0$ (Malfatti *et al.*, 2019).

The next set of figures show the composition of proto-neutron star matter for different combinations of entropy and lepton number, which characterize several different stages in the evolution of a hot, newly formed PNS to a cold NS. Proto-neutron stars in their earliest phases of evolution have $s = 1$ and $Y_L = 0.4$ followed by $s = 2$ and $Y_L = 0.2$. The particle compositions of such matter are shown in Figs. 1.10 through 1.13 for the DD2 and GM1L parametrizations. The matter in proto-neutron stars with $s = 2$ and $Y_L = 0.2$ undergoes deleptonization and becomes lepton poor. Such matter is characterized by $s = 2$ and $Y_{\nu_e} = 0$ (neutrinos are no longer present) and its compositions are shown in Figs. 1.14 and 1.15 for DD2 and GM1L, respectively. Finally, after several minutes stars with $s = 2$ and $Y_{\nu_e} = 0$ have cooled down to just ~ 1 MeV, containing core compositions similar to the one shown in Fig. 1.6.

One sees from Figs. 1.6 through 1.15 that both nuclear models, GM1L and DD2, predict the same overall particle compositions in hot and dense (proto-) neutron stars, despite the fact that the coupling constants of the models are treated quite differently. We recall that for the DD2 model the coupling constants of all (σ, ω, ρ) mesons are density dependent, while for the GM1L model this is only the case for the coupling constant of the ρ meson. A noteworthy difference, however, concerns the particle threshold densities which tend to be somewhat lower for the DD2 model.
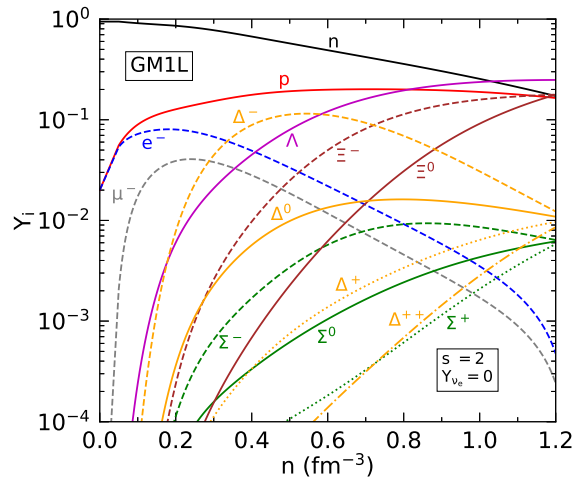
Fig. 1.15   Baryon-lepton composition of PNS matter obtained for GM1L model with $s = 2$ and $Y_{\nu_e} = 0$ (Malfatti *et al.*, 2019).

The temperature of PNS matter is shown in Figs. 1.16 and 1.17 for different combinations of entropy and lepton number. For a constant entropy density of $s = 1$ the temperature varies between around 15 and 18 MeV over most of the density ranges. The temperatures is more than twice as high for PNS matter with $s = 2$. Temperatures significantly higher than 40 MeV are not reached in PNS matter. The increase in temperature shown in these figures explains the ever more complex particle compositions shown in Figs. 1.10 through 1.15.

1.4   The Hadron-Quark Phase Transition

In this chapter, we briefly turn to the study of quark matter in compact stars. The possible existence of such matter in compact stars was already discussed in the 1960s by Ivanenko and Kurdgelaidze (1965) and in the 1970s by Itoh (1970); Fritzsch *et al.* (1973); Baym and Chin (1976); Keister and Kisslinger (1976); Chapline and Nauenberg (1977); Fechner and Joss (1978). Since then, a large number of scientific papers have been published describing the possible existence of quark matter in neutron stars with increasingly improved theoretical models (see, for instance, Page and Reddy (2006); Alford *et al.* (2008); Burgio and Plumari (2008); Bonanno, Luca and Sedrakian, Armen (2012); Orsaria *et al.* (2013, 2014); Baym, *et al.*
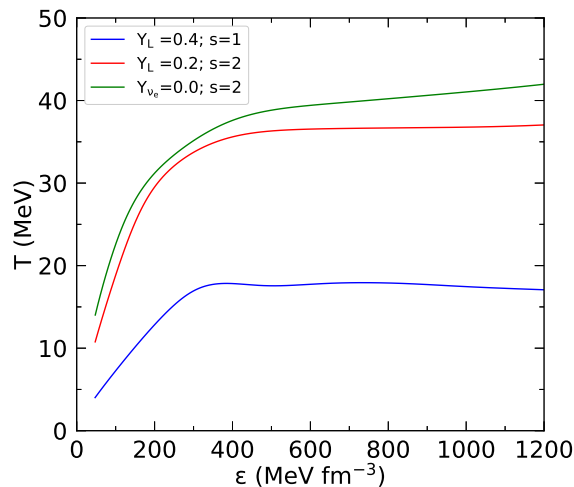
Fig. 1.16   Temperature as a function of energy density of PNS matter obtained for the DD2 model.

(2018); Blaschke and Chamel (2018); Tolos and Fabbietti (2020), and references therein). In the following we concentrate on the hadron-quark phase transition as described by the Nambu–Jona-Lasinio (NJL) model [Klevansky (1992); Hatsuda and Kunihiro (1994); Buballa (2005); Fukushima and Hatsuda (2011); Fukushima and Sasaki (2013)]. We shall use a non-local variant of the NJL model, denoted 3nPNJL, which includes vector interactions as well as the Polyakov loop. The lagrangian of this model is given by [Malfatti *et al.* (2019)]

$$
\mathcal{L} = \bar{\psi}(-i\gamma^\nu D_\nu + \hat{m})\psi + \frac{G_V}{2} j_a^\mu j_a^\mu - \frac{G_S}{2} \big[j_a^s j_a^s + j_a^p j_a^p \big]
$$
$$
- \frac{H}{4} A_{abc} \big[j_a^s j_b^s j_c^s - 3 j_a^s j_b^p j_c^p \big] + \mathcal{U}[\mathcal{A}], \tag{1.65}
$$

where $\mathcal{U}[\mathcal{A}]$ accounts for the Polyakov loop dynamics and the H-dependent term is the 't Hooft term responsible for quark flavor mixing. The quark fields are described by $\psi \equiv (u, d, s)^T$ and $\hat{m} = \mathrm{diag}(m_u, m_d, m_s)$ is the current quark mass matrix. The quantities j_a^μ, j_a^s, and j_a^p denote scalar (s), pseudo-scalar (p), and vector (μ) interaction currents, respectively, and G_S and G_V are the scalar and vector coupling constants. It is customary to express G_V in multiples of G_S and to write their ratio as $\zeta_v \equiv G_V/G_S$. The covariant derivative is given by $D_\nu \equiv \partial_\nu - igA_\nu^a t^a$, where A_ν^a are the gluon fields and $t^a = \lambda^a/2$ the generators of SU(3) (for more details, see
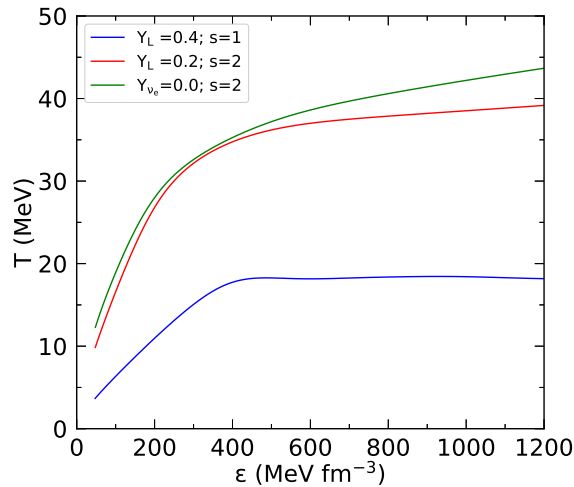
Fig. 1.17   Same as Fig. 1.16, but for the GM1L model.

Malfatti *et al.* (2019)).

To model the phase equilibrium between hadronic matter and quark matter in a neutron star, we assume here that this equilibrium is of first order and Maxwell-like, that is, the pressure in the mixed hadron-quark phase is constant. Theoretically the transitions could be Gibbs-like as well, depending on the surface tension at the hadron-quark interface. The value of the surface tension is however only poorly known. Lattice gauge calculations, for instance, predict surface tension values in the range of $0 - 100$ MeV fm^{-2} [Kajantie *et al.* (1991)]. Using different theoretical models for quark matter, a range of values for the hadron-quark surface tension have been obtained in the literature (see, for example, Refs. [Alford et al. (2001); Lugones et al. (2013); Ke and Liu (2014)], and references therein). According to theoretical studies, surface tensions above around 70 MeV fm^{-2} favor the occurrence of a sharp (Maxwell-like) hadron-quark phase transition rather than a softer Gibbs-like transition [Sotani *et al.* (2011); Yasutake *et al.* (2014)].

The EOS of both the hadronic phase and the quark phase is obtained from the Gibbs relation

$$\epsilon = -P + TS + \sum_i \mu_i \, n_i \,, \tag{1.66}$$

where pressure, entropy, and the particle number densities are given by $P =$
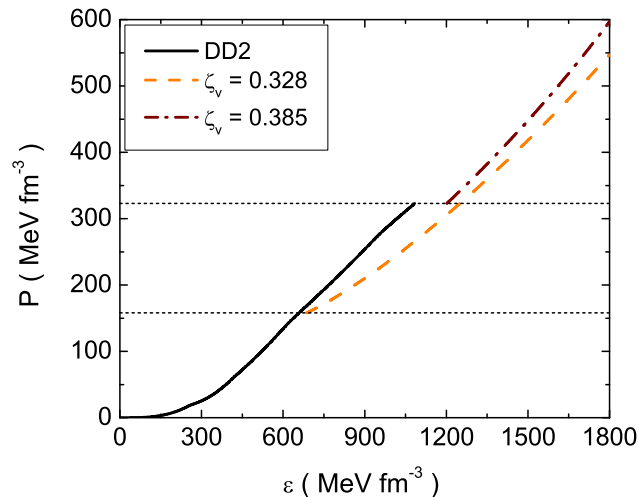
Fig. 1.18   Pressure as a function of the energy density for different values of the vector coupling constant ζ_{v} (see text) (Malfatti *et al.*, 2019). The black line represents the hadronic DD2 EOS and the dash-dotted and dashed lines are the EOSs of the quark (3nPNJL) phase for different ζ_{v} values. The horizontal lines mark the hadron-quark phase transitions.

$-\Omega$, $S = \frac{\partial P}{\partial T}$, and $n_i = \frac{\partial P}{\partial \mu_i}$, respectively. To construct the hadron-quark phase transition we adopt the Gibbs condition for equilibrium between both phases, expressed as

$$G_H(P,T) = G_Q(P,T)\,, \qquad (1.67)$$

where G_H and G_Q are the Gibbs free energies per baryon of the hadronic (H) and the quark (Q) phase, respectively, to be determined at a given pressure and transition temperature. The crossing of G_H and G_Q in the $G - P$ plane then determines the pressure and density at which the phase transition occurs for a given transition temperature. The expressions of G_H and G_Q are given by

$$G_i(P,T) = \sum_j \frac{n_j}{n} \mu_j\,, \qquad (1.68)$$

where $i = H$ or Q and the sum over j is over all the particles present in each phase. For the hadron-quark phase transition, the particle chemical potentials in each phase are different, so that is becomes necessary to calculate
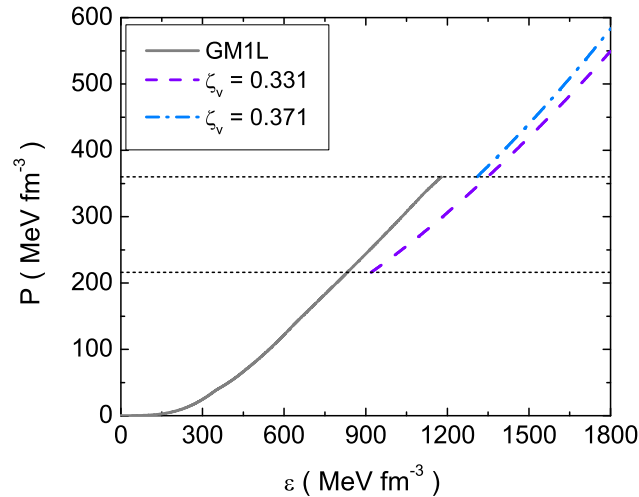
Fig. 1.19   Same as Fig. 1.18, but for the hadronic GM1L EOS (Malfatti *et al.*, 2019).

the Gibbs free energy as a function of pressure to construct the phase transition. Results for the hadron-quark phase transitions are shown in Fig. 1.18 for the DD2 nuclear model and in Fig. 1.19 for the GM1L nuclear model. Two phase transitions are visible in each figure, depending on the value of the vector coupling constant, ζ_v $(= G_V/G_S)$. The solid black and gray lines in these figures represent the hadronic DD2 and GM1L EOSs, respectively, and the dash-dotted and dashed lines are the EOSs of the quark phase computed for the 3nPNJL model. The horizontal lines indicate the locations of the hadron-quark phase transitions where $G_H(P, T = 0) = G_Q(P, T = 0)$ according to Eq. (1.67). The hadronic and the quark matter EOS are very similar at pressures where $G_H(P, T = 0) \approx G_Q(P, T = 0)$ [Malfatti *et al.* (2019)]). This makes it difficult to distinguish between the two phases in the relevant pressure regions, $P \sim 100 - 400$ MeV/fm^3. This can be interpreted as a masquerading behavior of dense matter, different from pure deconfined quark matter (see Malfatti *et al.* (2019), and references therein for details).

The $2\,M_\odot$ constraint of PSR J1614-2230 and PSR J0348+0432 [Demorest *et al.* (2010); Lynch *et al.* (2013); Antoniadis *et al.* (2013); Arzoumanian *et al.* (2018)] and the assumption that quark matter exists in the cores of neutron stars have been used to determine the range of the vector coupling
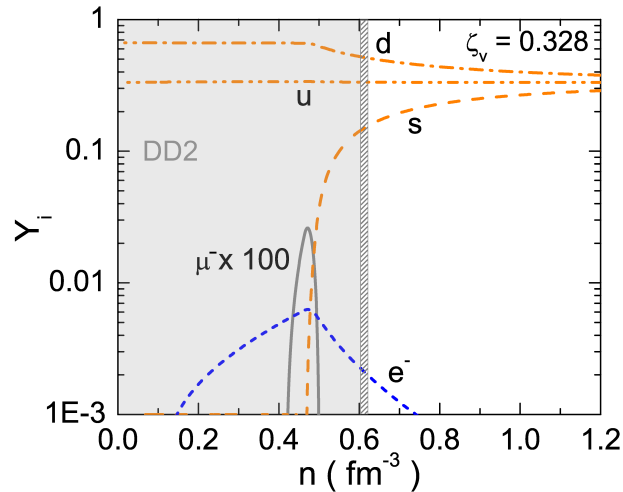
Fig. 1.20   Particle population of stellar quark matter at zero temperature as a function of baryon number density (Malfatti *et al.*, 2019). The gray area indicates the density regime where matter described by the hadronic DD2 model exists. The hadron phase ends abruptly at the vertical line slightly above 0.6 fm^{-3}. The population of muons is increased by a factor of 100 to make it visible. The strength of the vector repulsion among quarks is $\zeta_v = 0.328$.

constant ζ_v in the quark matter phase. This leads to $0.331 < \zeta_v < 0.371$ for GM1L, and $0.328 < \zeta_v < 0.385$ for DD2, where the lower bounds are determined by the $2\,M_\odot$ mass constraint and the upper bounds by the requirement that quark matter exists in the cores of neutron stars. In Figs. 1.20 and 1.21 we show the quark compositions of cold neutron stars computed for GM1L in combination with 3nPNJL and DD2 in combination with 3nPNJL, respectively.

1.5   The Parameters of the Hadronic Theory

For this study, we will consider three popular nuclear parametrization sets which are denoted SWL, GM1L and DD2 (Spinella, 2017; Spinella *et al.*, 2018; Typel *et al.*, 2010). The parameter values of these sets are shown in Table 1.1 and the corresponding saturation properties of symmetric nuclear matter are shown in Table 1.2 (Malfatti *et al.*, 2019). These are the nuclear
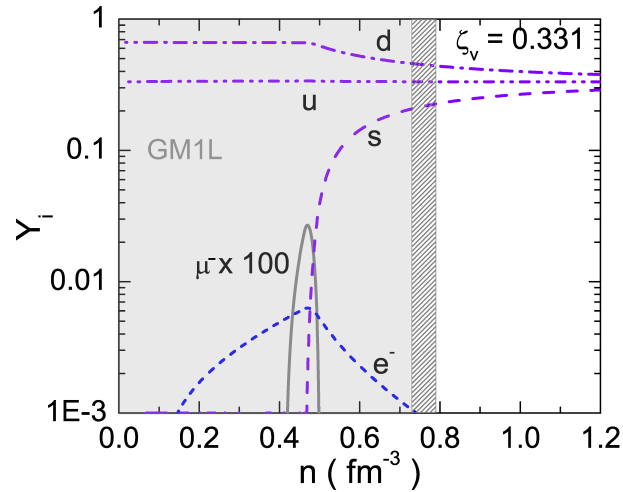
Fig. 1.21   Same as Fig. 1.20, but for a vector repulsion among quarks of $\zeta_v = 0.331$ (Malfatti *et al.*, 2019).

saturation density n_0, energy per nucleon E_0, nuclear compressibility K_0, effective nucleon mass m_N^*/m_N, asymmetry energy J, asymmetry energy slope L_0, and the value of the nucleon potential U_N. The values of L_0 listed in Table 1.2 are in agreement with the value of the slope of the symmetry energy deduced from nuclear experiments and astrophysical observations [Oertel *et al.* (2017)]. The DD2 parametrization is designed such that it eliminates the need for the nonlinear self-interactions of the σ meson shown in Eqs. (1.2) and (1.6) (Malfatti *et al.*, 2019). The nonlinear terms are therefore only considered for the GM1L model. As already mentioned in Sec. 1.2.1, the baryons considered in this study to populate NS matter include all states of the spin-$\frac{1}{2}$ baryon octet comprised of the nucleons (n, p) and hyperons $(\Lambda, \Sigma^+, \Sigma^0, \Sigma^-, \Xi^0, \Xi^-)$. In addition, all states of the spin-$\frac{3}{2}$ delta isobar $\Delta(1232)$ $(\Delta^{++}, \Delta^+, \Delta^0, \Delta^-)$ are taken into account as well.

Table 1.1   Parameters of the SWL and GM1L (Spinella, 2017; Spinella *et al.*, 2018) and DD2 (Typel *et al.*, 2010) parametrizations used in this work.

Parameters	Units	SWL	GM1L	DD2
m_σ	GeV	0.550	0.550	0.5462
m_ω	GeV	0.783	0.783	0.783
m_ρ	GeV	0.763	0.7700	0.7630
$g_{\sigma N}$	–	9.7744	9.5722	10.6870
$g_{\omega N}$	–	10.746	10.6180	13.3420
$g_{\rho N}$	–	7.8764	8.1983	3.6269
$\tilde{b}_\sigma$	–	0.003798	0.0029	0
$\tilde{c}_\sigma$	–	-0.003197	-0.0011	0
a_σ	–	0	0	1.3576
b_σ	–	0	0	0.6344
c_σ	–	0	0	1.0054
d_σ	–	0	0	0.5758
a_ω	–	0	0	1.3697
b_ω	–	0	0	0.4965
c_ω	–	0	0	0.8177
d_ω	–	0	0	0.6384
a_ρ	–	0.3796	0.3898	0.5189

1.5.1   *The Meson-Hyperon Coupling Space*

A detailed discussion of the meson-hyperon coupling constants g_{iH} (where $i = \sigma, \omega, \rho$) can be found in (Spinella, 2017; Malfatti *et al.*, 2019, 2020; Spinella and Weber, 2020). As usual we express the values of the meson-hyperon coupling constant, g_{iH}, in terms of the meson-nucleon coupling strength, g_{iN}, that is, $x_{iH} = g_{iH}/g_{iN}$. The meson-hyperon couplings are not well constrained experimentally compared to those of the nucleons. However, the scalar meson-hyperon couplings ($x_{\sigma H}$) can be constrained by the available experimental data on hypernuclei, but their calculation first requires the determination of the vector meson-hyperon couplings ($x_{\omega H}$). The coupling scheme used in our study is based on the Nijmegen extended-soft-core (ESC08) model (Rijken *et al.*, 2010). The scalar meson-hyperon coupling constants ($x_{\sigma H}$) can be fit to the hyperon potential depths, U_H at nuclear saturation density, n_0. Our parameters sets are fitted to potential depths of $U_\Lambda = -28$ MeV, $U_\Xi = -18$ MeV, and $U_\Sigma = +30$ MeV (see Schaffner-Bielich and Gal (2000); Spinella and Weber (2020); Tolos and Fabbietti (2020); Friedman and Gal (2021), and references cited therein). The values of the isovector meson-hyperon coupling constants are chosen as $x_{\rho H} = 2|I_{3H}|$ (Weissenborn *et al.*, 2012; Miyatsu *et al.*, 2013; Maslov

Table 1.2 Properties of symmetric nuclear matter at saturation density for the SWL and GM1L (Spinella, 2017; Spinella *et al.*, 2018) and DD2 (Typel *et al.*, 2010) parametrizations.

Saturation property	Units	SWL	GM1L	DD2
n_0	fm^{-3}	0.150	0.153	0.149
E_0	MeV	-16.0	-16.3	-16.02
K_0	MeV	260.0	300.0	242.7
m_N^*/m_N	$-$	0.70	0.70	0.56
J	MeV	31.0	32.5	32.8
L_0	MeV	55.0	55.0	55.3
U_N	MeV	-64.6	-65.5	-75.2

et al., 2016).

1.5.2 $\Delta(1232)$ *Isobars*

The potential presence of the delta isobar $\Delta(1232)$ in neutron star matter (Pandharipande, 1971; Sawyer, 1972; Boguta, 1982; Huber *et al.*, 1998) has been relatively ignored, especially when compared to the attention that hyperons have received in the literature. It is reasonable to assume Δs would not be favored in NS matter for a number of reasons. First, their rest mass is greater than both the Λ and Σ hyperons. Second, negatively charged baryons are generally favored as their presence reduces the high Fermi momenta of the leptons, but the Δ^- has triple the negative isospin of the neutron ($I_{3\Delta^-} = -3/2$), and thus its presence should be accompanied by a substantial increase in the isospin asymmetry of the system. However, these arguments now appear to be largely invalid since recent many-body calculations paint a different picture (Dexheimer and Schramm, 2008; Chen *et al.*, 2009; Schürhoff *et al.*, 2010; Lavagno, 2010; Drago *et al.*, 2014; Cai *et al.*, 2015; Zhu *et al.*, 2016; Spinella, 2017; Li *et al.*, 2018; Malfatti *et al.*, 2020).

Recent theoretical works have suggested conflicting constraints on the saturation potential of the Δs in symmetric nuclear matter given by

$$U_\Delta(n_0) = x_{\omega\Delta}g_{\omega N}\bar{\omega} - x_{\sigma\Delta}g_{\sigma N}\bar{\sigma} + \tilde{R}, \qquad (1.69)$$

where $\tilde{R}$ denotes the rearrangement term of Eq. (1.29). Drago *et al.* (2014) incorporated a number of experimental and theoretical results to deduce the following range for U_Δ at n_0,

$$-30\,\mathrm{MeV} + U_N(n_0) \lesssim U_\Delta(n_0) \lesssim U_N(n_0), \qquad (1.70)$$

indicating a slightly more attractive potential than that of the nucleons. Included in these analyses was an analysis of the photo-excitation of nucleons to Δs that suggested the following relation between the scalar and vector couplings,

$$0 < x_{\sigma\Delta} - x_{\omega\Delta} < 0.2 \,. \tag{1.71}$$

Kolomeitsev *et al.* (2017) cited numerous studies of Δ production in heavy ion collisions to suggest a less attractive potential in the range $U_N(n_0) \lesssim U_\Delta(n_0) \lesssim \frac{2}{3}U_N(n_0)$, finally settling on $U_\Delta(n_0) \approx -50$ MeV as a best estimate (Riek *et al.*, 2009). However, it is worth noting that constraining the potential does not directly constrain $x_{\sigma\Delta}$ or $x_{\omega\Delta}$, rather the relationship between the two.

The meson-Δ coupling space will be systematically investigated in Section 1.5.3, but first the particle number densities in the presence of both hyperons and Δs will be examined with the following set of couplings,

$$x_{\sigma\Delta} = x_{\omega\Delta} = 1.1, \;\; x_{\rho\Delta} = 1.0 \,. \tag{1.72}$$

These lead to saturation potentials more attractive than that of the nucleons as shown in Table 1.3. The scalar and isovector meson-hyperon coupling constants will continue to be determined as described in Sec. 1.5.1 and the vector meson-hyperon couplings will be given by the SU(3) ESC08 model.

The properties of maximum mass NSs made of hyperonic matter with and without the Δ states are shown in Table 1.4. The properties include the stellar mass M, the radius R, and the baryon number density n_c at the center of the stars. Also shown are the radii $R_{1.4}$ of neutron stars with a canonical mass of $1.4\,M_\odot$. As can be seen, including the Δ baryon actually leads to equal or marginally greater maximum masses in both cases. While the maximum masses are very similar, the mass-radius curves differ slightly due to the low density appearance of the Δ^- that causes a bend toward lower radii reducing the radius of the canonical $1.4\,M_\odot$ NS. We also note that specifying the vector meson-hyperon couplings with the SU(3) ESC08

Table 1.3 Saturation potentials of nucleons and Δs in symmetric nuclear matter with $x_{\sigma\Delta} = x_{\omega\Delta} = 1.1$ and $x_{\rho\Delta} = 1.0$ (Spinella, 2017).

Potential	SWL	GM1L	DD2
$U_N(n_0)$ (MeV)	-64.6	-65.5	-75.2
$U_\Delta(n_0)$ (MeV)	-71.1	-72.1	-86.0

Table 1.4 Properties of maximum mass NSs with Δs and hyperons with vector meson-hyperon coupling constants given in SU(3) symmetry with the ESC08 model (Spinella, 2017).

EOS	Hyperons				Hyperons plus Δs			
	M $(M_\odot)$	R (km)	n_c $(1/\text{fm}^3)$	$R_{1.4}$ (km)	M $(M_\odot)$	R (km)	n_c $(1/\text{fm}^3)$	$R_{1.4}$ (km)
SWL	2.01	11.5	0.98	12.80	2.02	11.4	1.00	12.85
GM1L	2.04	11.6	0.95	12.82	2.04	11.5	0.97	12.90
DD2	2.09	12.1	0.89	13.45	2.11	11.9	0.92	13.28

model rather than SU(6) is necessary in order to satisfy the $\sim 2\,M_\odot$ mass constraint with the GM1L and DD2 parametrizations (Spinella, 2017).

The relative particle number densities for the SU(3) coupling scheme are presented in Fig. 1.22 for the GM1L and DD2 parametrizations. For GM1L the Δ^- is the first additional baryon to be populated at $\sim 2.3\,n_0$ and reaches nearly the same number density as the proton before it starts being replaced by the Ξ^- at around $4\,n_0$. In DD2 the Δ^- again precedes the onset of hyperonization but appears at an extremely low baryon number density of around $1.8\,n_0$ and again reaches densities comparable to that of the pro-
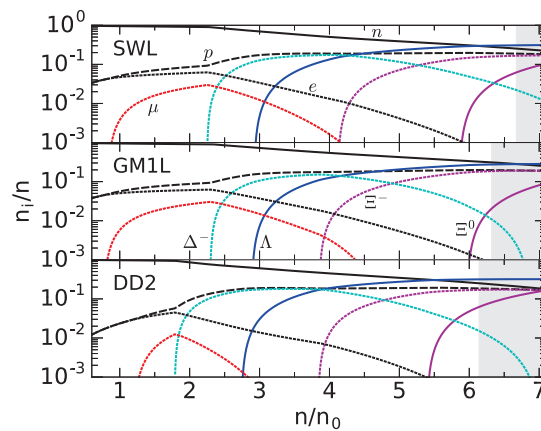

Fig. 1.22 The relative number density of particles in cold NS matter as a function of baryon number density (in units of the saturation density) (Spinella, 2017). The meson-Δ coupling constants are $x_{\sigma\Delta} = x_{\omega\Delta} = 1.1$, and $x_{\rho\Delta} = 1.0$, and the vector meson-hyperon coupling constants are given by the SU(3) ESC08 model. The gray shading indicates baryon number densities beyond the maximum for the given parametrization.

ton before beginning to decline due to the population of the Ξ^- at around $4\,n_0$. At low densities the Σ^- and Ξ^- may be disfavored in comparison to the Δ^- due to a repulsive potential and significantly higher rest mass respectively. However, the low Δ^- critical density in DD2 is primarily due to the density dependence of the isovector meson-baryon coupling that greatly reduces the isovector contribution to the Δ chemical potential compared to standard relativistic mean-field calculations. The early appearance of the Δ^- is directly related to the slope of the asymmetry energy, L_0, as discussed by Drago *et al.* (2014). The extreme low density appearance of the Δ^- has important consequences for the mass-radius curve of a NS, since it bends toward smaller radii much more substantially compared to EOSs where Δs are absent. The effect is the most drastic for the DD2 parametrization, where the presence of Δs reduces the canonical NS radius by about a kilometer compared to the nucleonic and hyperonic EOSs.

Figure 1.22 shows that the isospin neutral Λ is the first hyperon to appear at around $3\,n_0$, reducing the high Fermi momentum of the neutron. The isospin negative Ξ^- ($I_{3\Xi^-} = -1/2$) follows at around $4\,n_0$ as stated, replacing the more isospin negative Δ^- ($I_{3\Delta^-} = -3/2$), reducing isospin asymmetry. The isospin positive Ξ^0 ($I_{3\Xi^0} = +1/2$) is populated at around $6\,n_0$ in GM1L and $5.5\,n_0$ in DD2, contributing to the replacement of the isospin negative neutron further reducing isospin asymmetry. Finally, the presence of the Δ^- excludes the previous appearance of the Σ^- in DD2.

1.5.3   *The Meson-Δ(1232) Coupling Spaces*

Little empirical data exists that can unambiguously constrain the meson-Δ coupling constants. As a result, in order to study the presence of Δs in NS matter and their consequent effect on NS properties most studies choose just a few sets of coupling constants to analyze, typically in the vicinity of universal coupling ($x_{\sigma\Delta} = x_{\omega\Delta} = x_{\sigma\Delta} = 1$). In this section we seek to explore a large portion of the meson-Δ coupling space to more thoroughly investigate Δs in cold as well as hot (proto-) neutron star matter and their effect on stellar properties (Spinella, 2017; Malfatti *et al.*, 2020).

1.5.3.1   *The $\sigma\omega\Delta$ Coupling Space*

The exploration of the $\sigma\omega\Delta$ coupling space begins with a heatmap for the Δ saturation potential $U_\Delta(n_0)$ in symmetric nuclear matter given in Fig. 1.23. First, it is important to note that including the Δ baryon can result in a

rapid increase of the scalar field ($\bar{\sigma}$) causing a correspondingly rapid decrease in the effective baryon masses (see Eq. (1.20)), some becoming negative before the maximum central density is reached. This invalidates the EOS and the associated couplings; as a result, much of the $\sigma\omega\Delta$ coupling space is not accessible with a given EOS model and parametrization. These areas are identified in Fig. 1.23 and the heatmaps to follow as empty (white) pixels. Further, Δs do not populate for a significant region of the coupling space due to the presence of hyperons, and these couplings are identified by the gray pixels. In particular, we find that for the chosen parametrizations Δs are largely absent when $x_{\sigma\Delta} - x_{\omega\Delta} \lesssim -0.1$, and do not populate at all
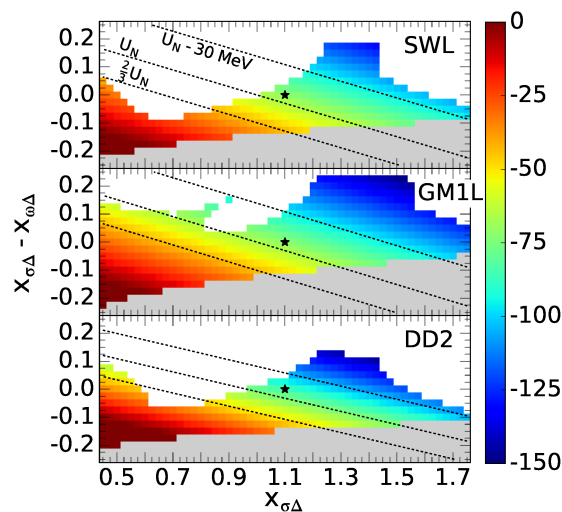

Fig. 1.23 Nuclear saturation potential (in MeV) of Δs in symmetric nuclear matter in the $\sigma\omega\Delta$ coupling space (Spinella, 2017). Hyperons were included with the vector meson-hyperon given by the SU(3) ESC08 model. The star marker indicates the location of $x_{\sigma\Delta} = x_{\omega\Delta} = 1.1$ and $x_{\rho\Delta} = 1.0$. Dashed contours are lines of constant potential as labeled and represent possible constraints. Gray pixels indicate that no Δs were populated for the given set of couplings. White pixels indicate couplings for which the effective mass of at least one baryon became negative before the maximum baryon number density of the NS was reached.

when $x_{\sigma\Delta} - x_{\omega\Delta} < -0.2$. A study by Zhu *et al.* (2016) investigated Δs in the density-dependent relativistic Hartree-Fock (DDRHF) approach, and much of the analysis therein was conducted with $x_{\sigma\Delta} = 0.8$ and $x_{\omega\Delta} = 1.0$. However, they did not account for hyperonization and our results suggest that Δs may not even appear with the given choice of couplings, illustrating

the importance of simultaneously considering hyperons. Finally, our investigation of the coupling range spanning $-0.25 \lesssim x_{\sigma\Delta} - x_{\omega\Delta} \lesssim 0.25$ appears sufficient, as outside this range Δs either do not populate or their presence results in an EOS that is erroneous due to either a negative effective baryon mass or a pressure that is not monotonically increasing. Thus, if Δs are to appear in NS matter, $x_{\sigma\Delta}$ and $x_{\omega\Delta}$ are likely relatively close in value.

Figure 1.23 indicates that an increase in either $x_{\sigma\Delta}$ or $x_{\sigma\Delta} - x_{\omega\Delta}$ results in a decrease in U_Δ, the potential becoming more attractive. The region between the top two contours is consistent with the potential constraint suggested by Drago *et al.* (2014) given in Eq. (1.70). Satisfaction of this constraint requires that $1.0 \lesssim x_{\sigma\Delta} \lesssim 1.7$ in SWL and DD2, and $0.9 \lesssim x_{\sigma\Delta} \lesssim 1.6$ in GM1L. Requiring that Eq. (1.71) be simultaneously satisfied completely excludes the bottom half of the coupling space and leaves only a limited region in the top-middle that is consistent with the constraints, this region including the previously employed couplings indicated by the star marker and given in Eq. (1.72). The region between the bottom two contours is consistent with the potential constraint suggested in Kolomeitsev *et al.* (2017). However, if we simultaneously require the satisfaction of Eq. (1.71) here the SWL and DD2 parametrizations are completely excluded, and the Δ couplings are limited to a very small range in the GM1L parametrization.

The maximum mass of NSs in the $\sigma\omega\Delta$ coupling space is shown in Fig. 1.24. The maximum mass constraint is satisfied by the majority of the meson-Δ coupling space in all parametrizations, with large regions producing a maximum mass greater than that of the purely hyperonic EOS with ESC08 vector couplings indicated by the solid contours. Consequently the maximum mass constraint alone does not serve to constrain $x_{\sigma\Delta}$ and $x_{\omega\Delta}$ significantly. The highest maximum masses appear where both the Δ saturation potential is the most attractive and the difference between the scalar and vector meson-Δ couplings is the greatest. Satisfaction of both Eq. (1.71) and the mass constraint requires $x_{\sigma\Delta} > 1.0$ for SWL, $x_{\sigma\Delta} > 0.9$ for GM1L, and $x_{\sigma\Delta} > 0.975$ for DD2. Kolomeitsev *et al.* (2017) concluded that the most likely value for $U_\Delta(n_0) \approx -50\,\mathrm{MeV}$, and we find that the maximum mass constraint can only be satisfied with this potential provided $x_{\omega\Delta} > x_{\sigma\Delta}$, violating Eq. (1.71) (Riek *et al.*, 2009; Kolomeitsev *et al.*, 2017).

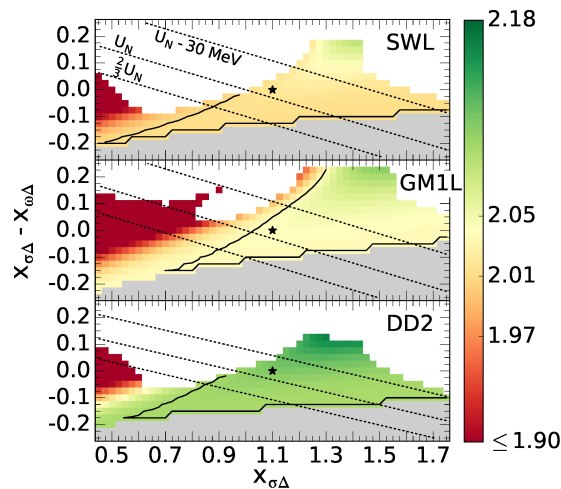The total number N_Δ of delta isobars present in a given NS model can

Fig. 1.24   Maximum mass (in solar mass units $M_\odot$) in the $\sigma\omega\Delta$ coupling space (Spinella, 2017). Hyperons were included with the vector meson-hyperon coupling constants given by the SU(3) ESC08 model. Solid lines are maximum mass contours for the associated hyperonic EOS (no Δs) in the ESC08 model. Colorbar tick marks represent the maximum mass constraints set by PSR J0348+0432 ($1.97-2.05\,M_\odot$ at 1σ, and $1.90-2.18\,M_\odot$ at 3σ). Markers, contours, and pixels are as described for Fig. 1.23.

be calculated from

$$\frac{dN_\Delta}{dr} = \frac{4\pi r^2}{\sqrt{1-2m(r)/r}}\sum_\Delta n_\Delta(r)\,, \qquad (1.73)$$

which is to be solved in combination with the TOV equation that will be introduced in Sec. 1.6. N_Δ is given in Fig. 1.25 as a fraction of the total baryon number, $f_\Delta = N_\Delta/N_B$. The Δ fraction varies considerably in the range $2\% \lesssim f_\Delta \lesssim 18\%$ when the $\sigma\omega\Delta$ couplings are consistent with the constraints given in Eq. (1.70) and Eq. (1.71). However, a quick examination of the same region in Fig. 1.24 reveals that this variance in f_Δ has little to no effect on the maximum stellar mass. It appears that there is a f_Δ hot-spot that is centered in a region of the $\sigma\omega\Delta$ coupling space inaccessible to the GM1L and DD2 EOS models, but the predictable result is that f_Δ increases with an increase in $x_{\sigma\Delta} - x_{\omega\Delta}$ when $x_{\sigma\Delta} \gtrsim 0.8$. The DD2 parametrization presents with the highest f_Δ for the smallest difference $x_{\sigma\Delta} - x_{\omega\Delta}$, followed by SWL and then GM1L.

The critical density n_{cr} for the appearance of Δs is shown in Fig. 1.26 for the $\sigma\omega\Delta$ coupling space. As long as Eq. (1.71) is satisfied, Δs appear prior to the onset of hyperonization, and $n_{\mathrm{cr}}^{\mathrm{SWL}} \lesssim 2.3\,n_0$, $n_{\mathrm{cr}}^{\mathrm{GM1L}} \lesssim 2.3\,n_0$, and
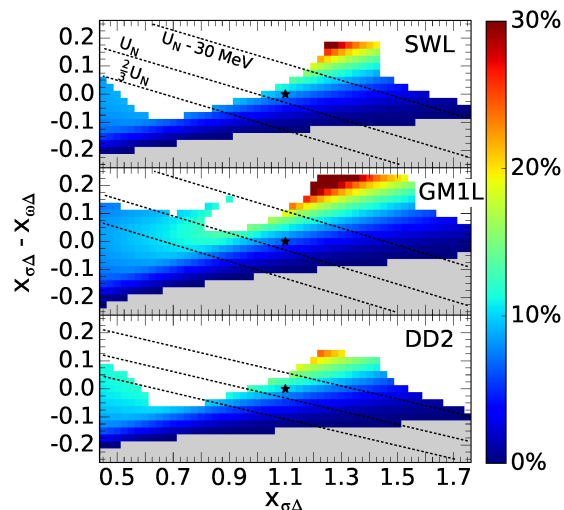
Fig. 1.25   Delta isobar fraction (percentage) of the maximum mass NS in the $\sigma\omega\Delta$ coupling space (Spinella, 2017). Hyperons were included with the vector meson-hyperon coupling constants given by the SU(3) ESC08 model. Markers, contours, and pixels are as described for Fig. 1.23. The Δ fractions for $x_{\sigma\Delta} = x_{\omega\Delta} = 1.1$ are as follows: $f_\Delta^{\text{SWL}} = 8.41\%$, $f_\Delta^{\text{GM1L}} = 6.31\%$, and $f_\Delta^{\text{DD2}} = 10.2\%$.

$n_{\text{cr}}^{\text{DD2}} \lesssim 1.9\,n_0$. If we also enforce simultaneous satisfaction of Eq. (1.70) the critical densities could be as low as $n_{\text{cr}}^{\text{SWL}} \approx 2\,n_0$, $n_{\text{cr}}^{\text{GM1L}} \approx 1.9\,n_0$, and $n_{\text{cr}}^{\text{DD2}} \approx 1.6\,n_0$. Increasing $x_{\sigma\Delta}$ leads to a gradual decrease in n_{cr} when $x_{\sigma\Delta} - x_{\omega\Delta} \gtrsim -0.1$, and a gradual increase in n_{cr} when $x_{\sigma\Delta} - x_{\omega\Delta} \lesssim -0.1$, the increase in the repulsive vector coupling overcoming the increasingly attractive potential in the latter case. However, increasing $x_{\sigma\Delta} - x_{\omega\Delta}$ leads to an obvious and rapid decrease in n_c for the entire $\sigma\omega\Delta$ coupling space, and if Eq. (1.71) is simultaneously satisfied an increase in $x_{\sigma\Delta} - x_{\omega\Delta}$ also leads to a significant reduction in the radius of the canonical $1.4\,M_\odot$ NS as shown in Fig. 1.27. For example, the DD2 parametrization with nucleons (and hyperons) produces a 13.5 km radius for the canonical $1.4\,M_\odot$ NS and thus fails to satisfy the 13.2 km upper-radial constraint from Lattimer and Steiner (2014), but if Δs are included and $x_{\sigma\Delta} > x_{\omega\Delta}$ the radius is reduced sufficiently to satisfy the constraint. If we allow Eq. (1.70) to be violated resulting in a very attractive U_Δ, the inclusion of Δs makes it possible for all three parametrizations to satisfy at least part of the 2σ upper limit on the radial constraints from Steiner *et al.* (2010).
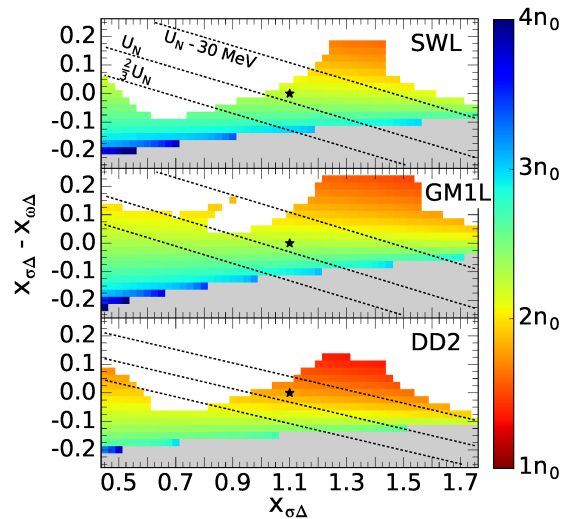
Fig. 1.26   Critical baryon number density (in units of n_0) for the appearance of Δs in the $\sigma\omega\Delta$ coupling space (Spinella, 2017). Hyperons were included with the vector meson-hyperon coupling constants given by the SU(3) ESC08 model. Markers, contours, and pixels are as described for Figure 1.23.

1.5.3.2   *The $x_{\rho\Delta}$ Coupling*

To examine the dependence of the NS mass, the Δ critical density $n_{\rm cr}$, and the Δ fraction f_Δ on the isovector meson-Δ coupling $x_{\rho\Delta}$ we set $x_{\sigma\Delta} = x_{\omega\Delta} = 1.1$ and varied $x_{\rho\Delta}$ in the range $0.5 < x_{\rho\Delta} < 2.5$ (Spinella, 2017). (Note that the saturation potential of the Δ is determined in symmetric nuclear matter and is therefore independent of $x_{\rho\Delta}$.) The NS maximum mass was found to not be terribly sensitive to $x_{\rho\Delta}$, decreasing over the entire range by less than 1% for the GM1L and DD2 parametrizations. However, $n_{\rm cr}$ and f_Δ turned out to be much more sensitive to changes in $x_{\rho\Delta}$ for the GM1L parametrization due to the fact that the isovector contribution to the chemical potential is much higher than for DD2. The critical density for GM1L increases from $\sim 2\,n_0$ to $\sim 3\,n_0$ across the entire $x_{\rho\Delta}$ range, with a corresponding drop in f_Δ of $\sim 8-9\%$ as this EOS reverts back to a nearly purely hyperonic EOS. The $n_{\rm cr}$ of the DD2 parametrization increases very little from around $1.7\,n_0$ to $1.9\,n_0$, but with an accompanying drop in f_Δ of almost 3% down to about 8%. Overall, lower values of $x_{\rho\Delta}$ lead to a lower critical density, resulting in higher fractions of Δs to replace hyperons and lower the strangeness fraction, increasing the NS maximum mass.
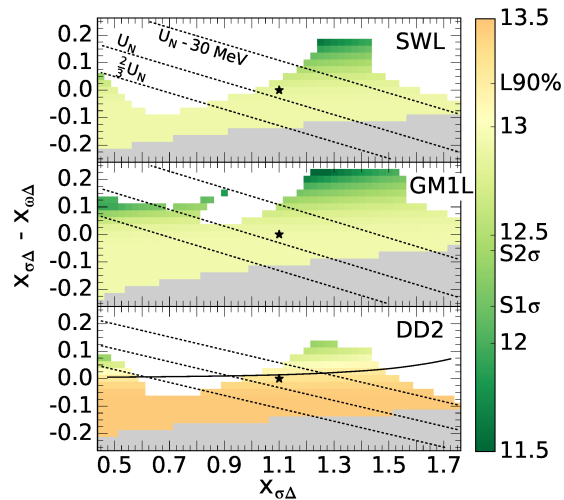
Fig. 1.27   Radius (in km) of the canonical $1.4\,M_\odot$ NS in the $\sigma\omega\Delta$ coupling space (Spinella, 2017). Hyperons were included with the vector meson-hyperon coupling constants given by the SU(3) ESC08 model. The solid contour in the bottom (DD2) panel represents the 13.2 km upper limit of the radial constraint from Lattimer and Steiner (2014) represented as L90% on the colorbar. The 1σ and 2σ upper limits from Steiner *et al.* (2010) are represented on the colorbar as S1σ and S2σ respectively. Markers, dashed contours, and pixels are as described for Fig. 1.23.

1.6   General Relativistic Stellar Structure Equations

Neutron stars are objects of highly compressed matter so that the geometry of surrounding space-time is changed considerably from flat space. Einstein's theory of general relativity is therefore to be used when modeling the properties of NSs rather than Newtonian mechanics. Einstein's field equation is given by (we use units where the gravitational constant and the speed of light are $G = c = 1$)

$$R^{\mu\nu} - \frac{1}{2}g^{\mu\nu}R = 8\pi T^{\mu\nu}\,, \tag{1.74}$$

where $R^{\mu\nu}$ is the Ricci tensor, $g^{\mu\nu}$ the metric tensor, R the scalar curvature, and $T^{\mu\nu}$ the energy-momentum tensor of matter. The latter is given by

$$T^{\mu\nu} = \left(\epsilon + P(\epsilon)\right)u^\mu u^\nu + g^{\mu\nu}P(\epsilon)\,. \tag{1.75}$$

Models for the EOS, $P(\epsilon)$, which are input quantities in the energy-momentum tensor equation, have been derived in Sec. 1.2. These models will be used in this section to study the properties of NSs.

1.6.1 *Non-rotating Proto-Neutron Stars*

We begin with non-rotating, spherically symmetric NSs. They are relatively easy to study since the metric of such objects depends only on the radial coordinate. The line element ds^2 in this case is given by the Schwarzschild metric (Schwarzschild, 1916; Misner *et al.*, 1973; Shapiro and Teukolsky, 2008)

$$ds^2 = -e^{2\,\Phi(r)}dt^2 + e^{2\,\Lambda(r)}dr^2 + r^2\left(d\theta^2 + \sin^2\theta\,d\phi^2\right), \qquad (1.76)$$

where $\Phi(r)$ and $\Lambda(r)$ denote unknown metric functions whose mathematical form is determined by Einstein's field equation Eq. (1.74) and the conservation of energy-momentum, $\nabla_\mu T^{\mu\nu} = 0$, and have the form

$$e^{2\,\Lambda(r)} = \left(1 - \frac{2m(r)}{r}\right)^{-1} \qquad \text{(inside and outside of star)}, \qquad (1.77)$$

$$e^{2\,\Phi(r)} = \left(1 - \frac{2m(r)}{r}\right) \qquad \text{(only outside of star)}. \qquad (1.78)$$

The solution of $\Phi(r)$ for the stellar interior is given by

$$\frac{d\Phi(r)}{dr} = -\frac{1}{\epsilon + P(\epsilon)}\frac{dP(r)}{dr}, \qquad (1.79)$$

where the pressure gradient is given by the Tolman-Oppenheimer-Volkoff (TOV) equation (Oppenheimer and Volkoff, 1939; Tolman, 1939; Misner *et al.*, 1973),

$$\frac{dP}{dr} = -\frac{\left(\epsilon(r) + P(r)\right)\left(m(r) + 4\pi r^3 P(r)\right)}{r^2\left(1 - 2m(r)/r\right)}. \qquad (1.80)$$

The quantity $m(r)$ in Eq. (1.80) denotes the gravitational stellar mass given by

$$m(r) = 4\pi \int_0^r dr\, r^2\, \epsilon(r). \qquad (1.81)$$

The boundary condition associated with Eq. (1.80) specifies the pressure at the stellar center, $P(r = 0)$. Equation (1.80) is integrated, for a given EOS, outward to a radial distance where the pressure vanishes (turns negative). This defines the radius, R, of the stellar model and the star's total gravitational mass is then given by $M \equiv m(R)$. Figures 1.28 and 1.29 show M as a function of R of proto-neutron stars computed for the DD2 and GM1L models for the nuclear EOS. The most massive stars of our sample are those with an entropy per baryon of $s = 1$ and a lepton fraction of $Y_L = 0.4$, since the matter in their cores provides the most pressure (see Figs. 1.2 and 1.3)
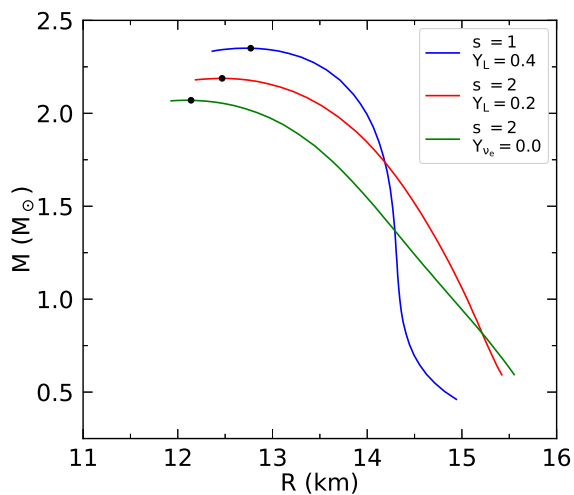
Fig. 1.28   Mass-radius relationships of PNS computed for the DD2 parametrization.

Fig. 1.29   Same as Fig. 1.28, but computed for the GM1L nuclear parametrization.

of all the entropy–lepton number combinations investigated in this work. The EOS computed for $s = 2$ and $Y_{\nu_e} = 0$ provides the least amount of pressure (i.e., is the softest EOS of our collection) and therefore leads to the least massive stars. We note that the mass-radius curves of all stars lighter

than $\sim 1\, M_\odot$ are not reliable since temperature effects on the matter of the stellar crust have not been taken into account in our calculations.

1.6.2 *Rotating Proto-Neutron Stars*

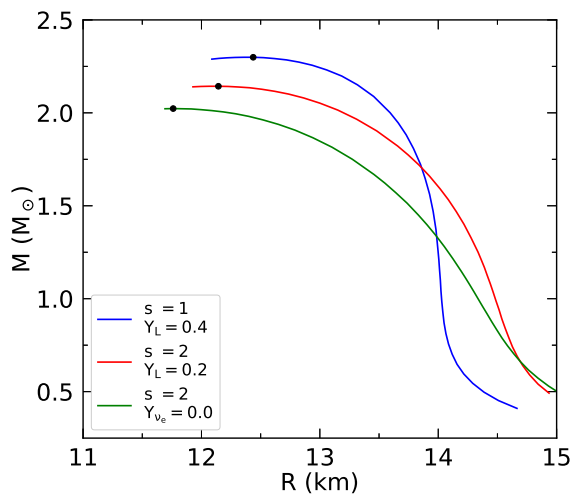The properties of rotating compact objects are much more complicated to study than those of non-rotating compact objects. This has its origin in the fact that due to rotation the stars are deformed (so that the metric functions depend on the polar angle θ) as well as the dragging of the local inertial frames, which is caused by rotating systems in the general theory of relativity. The line element accounting for these effects is given by (Butterworth and Ipser, 1976; Friedman *et al.*, 1986)

$$ds^2 = -\, e^{2\,\nu(r,\theta,\Omega)}\, dt^2 + e^{2\,\psi(r,\theta,\Omega)}\, (d\phi - \omega(r,\Omega)\, dt)^2 + e^{2\,\mu(r,\theta,\Omega)}\, d\theta^2 $$
$$+ e^{2\,\lambda(r,\theta,\Omega)}\, dr^2\,. \tag{1.82}$$

Here, ω is the angular frequency of the local inertial frames which depends on the radial coordinate, r, and on the star's rotational frequency Ω. We take Ω to be constant throughout the star's fluid (rigid-body rotation). Of particular interest in the discussion of rotating compact objects is the effective angular frequency $\bar{\omega} \equiv \Omega - \omega$, which is the angular frequency of the stellar fluid relative to the local inertial frames.

1.6.2.1 *The General Relativistic Kepler Frequency*

No simple stability criteria are known for rotating star configurations in general relativity. An absolute upper limit on rapid rotation, is however set by the Kepler frequency Ω_{K}, at which mass shedding from a star's equator sets in. The expression of the general relativistic Kepler frequency is derived from the line element shown in Eq. (1.82), evaluated at the equator of a compact stellar object. Since $dr = 0$ and $d\theta = 0$ for a mass element rotating at the equator, one obtains from Eq. (1.82) for the proper time $d\tau^2\ (= -ds^2)$ the relation

$$d\tau = \left(e^{2\,\nu(r,\theta,\Omega)} - e^{2\,\psi(r,\theta,\Omega)}\,(\Omega - \omega(r,\theta,\Omega))^2\right)^{1/2} dt\,. \tag{1.83}$$

The equatorial orbit, which is the circular path with the maximum possible distance from the center of a gravitating body, is obtained from Eq. (1.83) by determining the extremum of the functional $J(r)$ associated with Eq. (1.83), that is,

$$J(r) \equiv \int dt\, \left(e^{2\,\nu(r,\theta,\Omega)} - e^{2\,\psi(r,\theta,\Omega)}\,(\Omega - \omega(r,\theta,\Omega))^2\right)^{1/2}\,. \tag{1.84}$$

Applying the extremal condition $\delta J(r) = 0$ to this functional leads to

$$\delta \int dt \, \left(\mathrm{e}^{2\,\nu(r,\theta,\Omega)} - \mathrm{e}^{2\,\psi(r,\theta,\Omega)} \, (\Omega - \omega(r,\theta,\Omega))^2 \right)^{1/2} = 0 \,, \qquad (1.85)$$

from which it follows that (Weber, 1999)

$$\int dt \, \delta r \, \frac{\nu_{,r} \, \mathrm{e}^{2\,\nu} - (\psi_{,r} \, (\Omega - \omega) - \omega_{,r}) \, (\Omega - \omega) \, \mathrm{e}^{2\,\psi}}{\left(\mathrm{e}^{2\,\nu} - \mathrm{e}^{2\,\psi} (\Omega - \omega)^2 \right)^{1/2}} = 0 \,. \qquad (1.86)$$

For the sake of brevity, we suppress all arguments here and in the following. The subscripts $_{,r}$ on the metric functions and the frame dragging frequency in Eq. (1.86) denote partial derivatives with respect to the radial coordinate, r. Next, we introduce the orbital velocity V of a co-moving observer at the star's equator relative to a locally non-rotating observer with zero angular momentum in the ϕ-direction. This velocity is given by

$$V = \mathrm{e}^{\psi - \nu} \, (\Omega - \omega) \,. \qquad (1.87)$$

This relation is suggested by the expression of the time-like component u^t of the four-velocity of a mass element rotating in the equatorial plane,

$$u^t = \frac{dt}{d\tau} = \mathrm{e}^{-\nu} \, \left(1 - V^2 \right)^{-1/2} \,, \qquad (1.88)$$

where V is given by Eq. (1.90). Substituting Eq. (1.87) into Eq. (1.86) then leads to

$$\psi_{,r} \, \mathrm{e}^{2\,\nu} \, V^2 - \omega_{,r} \, \mathrm{e}^{\nu + \psi} \, V - \nu_{,r} \, \mathrm{e}^{2\,\nu} = 0 \,, \qquad (1.89)$$

which guarantees that the integrand in Eq. (1.86) vanishes identically for arbitrary variations δr. Equation (1.89) represents a quadratic equation for the velocity V. The solutions are given by (Friedman *et al.*, 1986)

$$V = \frac{\omega_{,r}}{2 \, \psi_{,r}} \, \mathrm{e}^{\psi - \nu} \pm \left(\frac{\nu_{,r}}{\psi_{,r}} + \left(\frac{\omega_{,r}}{2 \, \psi_{,r}} \, \mathrm{e}^{2(\psi - \nu)} \right)^2 \right)^{1/2} \,. \qquad (1.90)$$

The general relativistic Kepler frequency, Ω_{K}, is then obtained from (cf. Eq. (1.87)) as

$$\Omega_{\mathrm{K}} = \mathrm{e}^{\nu - \psi} \, V + \omega \,. \qquad (1.91)$$

We note that Eqs. (1.90) and (1.91) need to be computed self-consistently together with Einstein's field equations, which determined the metric functions ν and ψ and the frame dragging frequency ω at an (initially unknown) equatorial distance. The result of classical Newtonian mechanics for the Kepler frequency and the velocity of a particle in a circular orbit, $\Omega_{\mathrm{K}} = \sqrt{M/R^3}$ and $V = R\Omega$ respectively, are recovered from Eqs. (1.90)
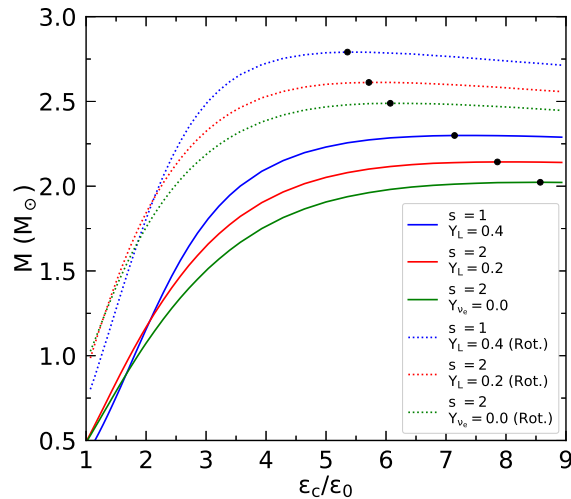
Fig. 1.30   Gravitational mass of PNSs as a function of central energy density in units of the energy density of ordinary nuclear matter ($\epsilon_0 = 140 \text{ MeV/fm}^3$) computed for GM1L.

and (1.91) by neglecting the curvature of space-time geometry, the rotational deformation of a rotating star, and the dragging effect of the local inertial frames.

Figure 1.30 shows the impact of rapid rotation on the gravitational masses of proto-neutron stars. The solid lines in this figure show the masses of non-rotating (i.e., TOV) stars. The dashed lines reveal by how much these masses increase if the stars are rotating at the highest possible spin rate, which is the Kepler frequency given by (1.91). The increase in mass of cold NSs is typically at the 20% level, depending on the EOS (Friedman *et al.*, 1986). The same is the case for the gravitational masses of proto-neutron stars, as can be inferred from Fig. 1.30. We also note that the stars' central energy density, ϵ_c, decreases with rotation speed, because of the additional rotational pressure in the radial outward direction created by rotation.

As mentioned just above, to find the Kepler frequency $\Omega_{\rm K}$ (Kepler period, $P = 2\pi/\Omega_{\rm K}$) of a compact star, Eqs. (1.90) and (1.91) and are to be computed self-consistently in combination with the differential equations for the metric and frame-dragging functions in Eq. (1.82), which follow from Einstein's field equation (1.74). The entire set of coupled equations is to be evaluated at the equator of the rotating star (Friedman *et al.*, 1986;

Weber and Glendenning, 1992), which is not known at the beginning of the computational procedure. Here, the results of stars rotating at the Kepler period are computed in the framework of Hartle's perturbative rotation formalism (Weber and Glendenning, 1992). The latter constitute a perturbative approach to Einstein's field equations, that leads to results that are in very good agreement with those obtained by numerically exact treatments of Einstein's field equations. This is particularly the case for the mass increase due to fast rotation and the value of the Kepler frequency.

Figure 1.31 shows that the maximum possible rotational (Kepler) speed at the equator of PNSs is around $0.7\,c$. This value depends only mildly on the actual stellar composition. One also sees that the hottest of the three stellar families (green line) terminates (solid black dot) at an equatorial speed that is smaller than the speed of the other two sequences. This has its origin in the fact that $s = 2$ and $Y_{\nu_e} = 0$ PNSs have the highest temperatures of all three configurations and thus the biggest radii, so that mass-shedding from the equator sets in first in these stars.

The Kepler periods of the rotating PNSs of Figs. 1.30 through 1.31 are displayed in Fig. 1.32. Based on the results shown in this figure, we conclude that PNSs posses about the same Kepler periods as cold neutron stars.

1.6.2.2   *Gravitational Radiation-Reaction Driven Instabilities*

Besides the absolute upper limit on rapid rotation set by the Kepler frequency, there are other instabilities that have been shown to set in at a lower rotational frequency, and which therefore set more stringent limits on stable rotation (Lindblom, 1986; Owen *et al.*, 1998; Andersson *et al.*, 1999; Andersson and Kokkotas, 2001; Lin *et al.*, 2021). They typically originate from counter-rotating surface vibrational modes, which at sufficiently high rotational star frequencies are dragged forward. In this case, gravitational radiation which inevitably accompanies the aspherical transport of matter does not damp the modes, but rather drives them (Chandrasekhar, 1970; Friedman, 1983b,a). Bulk and shear viscosity play the important role of damping such gravitational-wave radiation-reaction instabilities at a sufficiently reduced rotational frequency such that the viscous damping rates and power in gravity waves are comparable (Lindblom and Detweiler, 1977; Andersson and Kokkotas, 2001). Theoretical studies suggest that either the f-modes or the r-modes determine the maximum rotation frequency of neutron stars.
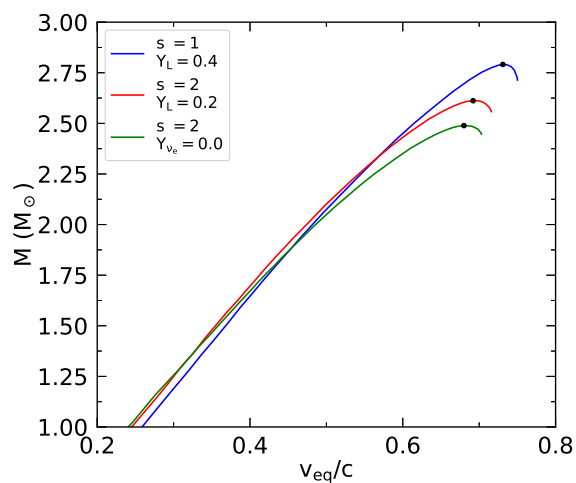
Fig. 1.31   Gravitational mass of rotating PNSs versus equatorial speed for GM1L EOS.
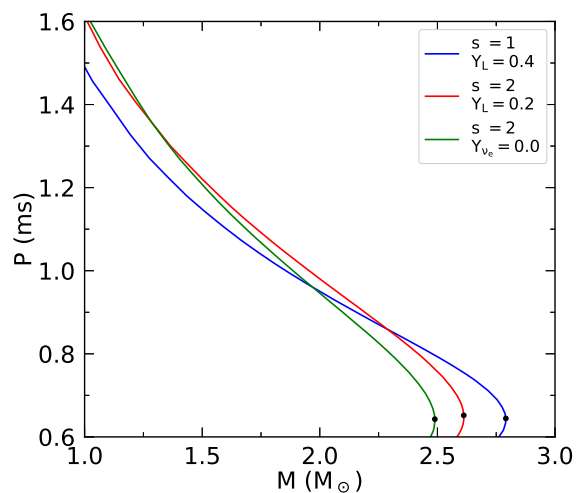

Fig. 1.32   Kepler periods of rotating PNs versus gravitational mass for the GM1L EOS.

1.6.3   *The Moment of Inertia*

Another very important stellar quantity, which will be discussed in this section, is the moment of inertia, I. This quantity is given by [Hartle

(1973)]

$$I(\Omega) = \frac{1}{\Omega} \int_A dr\, d\theta\, d\phi\; T_\phi{}^t(r,\theta,\phi;\Omega)\; (-g(r,\theta,\phi;\Omega))^{1/2} \,, \qquad (1.92)$$

where A denotes the region inside of a compact stellar object rotating at a uniform angular velocity, Ω. The quantity g denotes the determinant of the metric tensor $g_{\mu\nu}$, whose components can be read off from Eq. (1.82). One obtains (Weber, 1999)

$$\sqrt{-g} = e^{\lambda+\mu+\nu+\psi} \,. \qquad (1.93)$$

The energy-momentum tensor component $T_\phi{}^t$ is given by (see Eq. (1.75))

$$T_\phi{}^t = (\epsilon + P)\, u_\phi\, u^t \,, \qquad (1.94)$$

with the four-velocities u_ϕ and u^t given by

$$u^t = \frac{e^{-\nu}}{\left(1 - (\omega - \Omega)^2\, e^{2\psi-2\nu}\right)^{1/2}} \,, \qquad (1.95)$$

$$u_\phi = (\Omega - \omega)\, e^{2\,\psi}\, u^t \,. \qquad (1.96)$$

Substituting Eqs. (1.95) and (1.96) into Eq. (1.94) leads for $T_\phi{}^t$ to

$$T_\phi{}^t = \frac{(\epsilon + P)\,(\Omega - \omega)\, e^{2\,\psi}}{e^{2\,\nu} - (\omega - \Omega)^2\, e^{2\,\psi}} \,. \qquad (1.97)$$

Substituting the expression given in Eq. (1.93) and Eq. (1.97) into Eq. (1.92) leads for the moment of inertia of a rotationally deformed compact stellar object to (Weber, 1999)

$$I(\Omega) = 2\pi \int_0^\pi d\theta \int_0^{R(\theta)} dr\, e^{\lambda+\mu+\nu+\psi}\, \frac{\epsilon + P(\epsilon)}{e^{2\nu-2\psi} - (\omega - \Omega)^2}\, \frac{\Omega - \omega}{\Omega} \,. \quad (1.98)$$

In Figs. 1.33 and 1.34 we show the results for the moment of inertia computed for the DD2 and GM1L nuclear parametrizations. As can be seen, massive PNSs with $s = 1$ and $Y_L = 0.4$ posses the largest moments of inertia, followed by PNS with $s = 2$ and $Y_L = 0.2$, and $s = 2$ and $Y_{\nu_e} = 0.0$. This trend is consistent with the stiffness of the PNS equations of state shown in Figs. 1.2 through 1.5, the associated mass-radius relationships shown in Figs. 1.28 and 1.29, and the mass-central density curves shown Fig. 1.30. Figures 1.33 and 1.34 show that $2\,M_\odot$ PNSs, for instance, possess moments of inertia of around 270 km^3. It is interesting to compare this value with the moment of inertia of a spherical uniform mass distribution in Newtonian physics, which is given by $I = \frac{2}{5}MR^2 = \frac{3}{5}\left(\frac{M}{M_\odot}\right)\left(\frac{R}{\text{km}}\right)^2$ km^3. This gives values for I for the $2\,M_\odot$ PNSs in Figs. 1.28 and 1.29 which
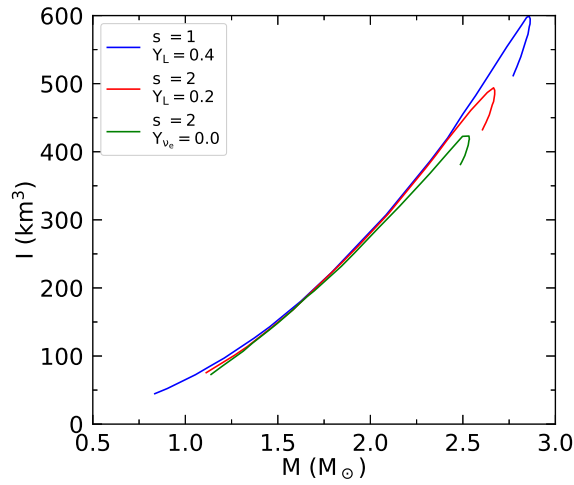
Fig. 1.33   Moment of inertia versus gravitational mass, for the DD2 parameter set.
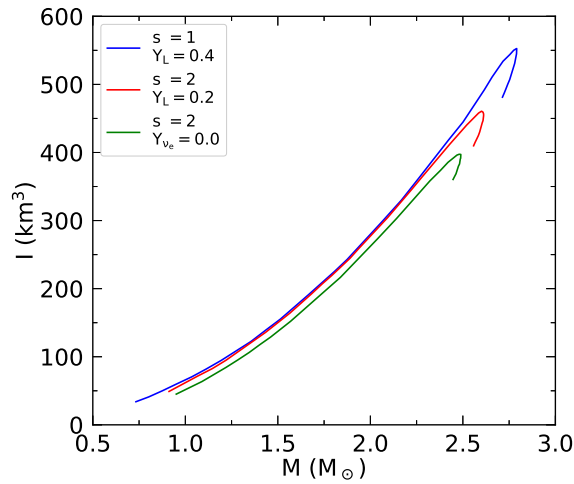
Fig. 1.34   Same as Fig. 1.33, but for the GM1L parameter set.

are between 175 km^3 and 235 km^3. These values are on the same order of magnitude as the general relativistic results, but differ significantly quantitatively. Sudden changes ΔI in the moments of inertia of (proto-) neutron stars are expected to lead to sudden changes $\Delta \Omega$ in the spin frequencies of such objects. Assuming angular momentum conservation during such

episodes, the change in spin frequency may be estimated as

$$\frac{\Delta\Omega}{\Omega} = -\frac{\Delta I}{I + \Delta I} \,, \tag{1.99}$$

where Ω is the frequency of the star before the change in the moment of inertia. Observed changes in the spin frequencies of rotating neutron stars (pulsars) range from 10^{-6} to 10^{-9} and have been suggested to originate from sudden decreases in the moments of inertia of such objects (Lyne, 1992; Fuentes, J. R. *et al.*, 2017; Manchester, 2017; Montoli *et al.*, 2022). Similar arguments have been used by Garcia and Ranea-Sandoval (2015) and Mastrano et al. (2015) to explain the anti-glitch observed for the magnetar AXP 1E 2259+586 [Archibald et al. (2013)]. Equation (1.99) indicates that already $|\Delta I| \sim 10^{-6}$ km^3 to 10^{-9} km^3 could suffice to cause such changes. This is also the reason why the nuclear crust on hypothetical strange quark stars could explain the observed pulsar glitches [Glendenning and Weber (1992)].

1.7 Future Directions of Research

It is often stressed that there has never been a more exciting time in the overlapping areas of nuclear physics, particle physics, relativistic astrophysics and astronomy than today. This interest is stimulated by investments made in international nuclear physics facilities such as FAIR, FRIB, NICA, CERN, BNL, J-Park and multiple new instruments for sky surveys that have become operational in recent years, such as FAST, eROSITA, NICER and the gravitational-wave detectors LIGO, VIRGO, KAGRA. In particular, the observation of the first binary neutron star merger, GW170817, using LIGO and VIRGO (Abbott, 2017) have led the scientific community into the new era named multi-messenger astronomy with gravitational waves.

Depending on the combined masses of two merging NSs, there are in principle four possible outcomes to a merger (Chirenti *et al.*, 2019): 1) prompt formation of a black hole, 2) formation of a hypermassive NS (HMNS) (Baumgarte *et al.*, 2000; Shapiro, 2000), 3) formation of a supramassive rotating NS (Falcke and Rezzolla , 2014), or 4) the formation of a stable NS. Numerical relativity simulations have shown that the threshold masses related to these scenarios depend strongly on the properties and the EOS of hot and dense NS matter. (For a comprehensive review of the physics of NS mergers, see Baiotti and Rezzolla (2017), and references therein.) The same is true for the lifetime of HMNSs, which depends

strongly on the total mass of the binary system and, thus, on the nuclear EOS. The post-merger emissions are typically characterized by two distinct frequency peaks, one at high and the other at lower frequencies. The EOS dependent high-frequency peak is believed to be associated with the oscillations of the HMNS produced in a merger, while the low-frequency peak is understood to be related to the merger process and to the total compactness (i.e., mass-radius ratio) of the merging objects (Takami *et al.*, 2015), which is inexorably linked to the EOS of dense nuclear matter.

The EOS of cold and dense nuclear matter is sufficient to describe NS matter prior to a NS merger. After contact, however, large shocks develop which considerably increase the internal energy of the colliding NSs. Numerical simulations have shown that overall matter in NS collisions reaches densities that are several times higher than the nuclear saturation density and temperatures that are roughly as high as 50 MeV (Baiotti and Rezzolla, 2017; Hanauske *et al.*, 2019a; Perego, Albino *et al.*, 2019). As shown in this chapter, such extreme conditions of density and pressure modify the EOS and in particular the baryon-lepton composition of the matter tremendously.

Very recently, is has been shown that a strong first-order phase transition in NS mergers may register itself in the gravitational-wave frequency, f_{peak}, and the stellar tidal deformability, Λ [Bauswein *et al.* (2019)]. Since both the tidal deformability during inspiral and the oscillation frequencies of the post-merger remnant can be determined very reliably [Faber and Rasio (2012); Baiotti and Rezzolla (2017); Paschalidis and Stergioulas (2017); Friedman (2018); Duez and Zlochower (2018)], this finding relates NS merger simulations to the general science question whether or not phase transitions occur in dense nuclear matter. Signatures of possible hadron-quark phase transitions in NS mergers have also been studied by Most *et al.* (2019). This study shows that changes in the pressure of the quark phase can produce a decisive signature in the post-merger gravitational-wave signal and spectrum. It was also shown that a hadron-quark phase transition may lead to a hot and dense quark core which could produce a ring-down signal different from what is expected for a pure hadronic core. The possibility of detecting the hadron-quark phase transition with gravitational waves has been discussed recently by Hanauske *et al.* (2019b).

A great deal of experimental, theoretical as well as computational work will need to be carried out over the coming years to determine a comprehensive class of state-of-the-art models for the EOS of ultra-hot and dense nuclear matter for use in binary NS merger simulations and PNS simu-

Book Title

lations (Shen *et al.*, 2011; Rezzolla and Olindo, 2013; Banik *et al.*, 2014; Hanauske *et al.*, 2019b).

Acknowledgments

Bibliography

Abbott, B. P. *et al.*. (2017). *GW170817: Observation of gravitational waves from a binary neutron star inspiral, Phys. Rev. Lett.* **119**, pp. 161101.

Alford, M., Rajagopal, K., Reddy, S., Wilczek, F. (2001). *Minimal color-flavor-locked-nuclear interface*, *Phys. Rev. D* **64**, p. 074017.

Alford, M. G., Schmitt, A., Rajagopal, K., and Schäfer, T. (2008). Color superconductivity in dense quark matter, *Rev. Mod. Phys.* **80**, pp. 1455–1515.

Andersson, N., Kokkotas, K., and Schutz, B. F. (1999). *Gravitational radiation limit on the spin of young neutron stars, Astrophys. J.* **510**, 2, pp. 846–853.

Andersson, N. and Kokkotas, K. D. (2001). *The r-mode instability in rotating neutron stars, Int. J. Mod. Phys. D* **10**, pp. 381–441.

Antoniadis, J. *et al.* (2013). *A Massive Pulsar in a Compact Relativistic Binary, Science* **340**, pp. 6131.

Archibald, R. F. *et al.* (2013). *An anti-glitch in a magnetar. Nature* **497**, pp. 591—593.

Arzoumanian, Z., Brazier, A., Burke-Spolaor, S., Chamberlin, S., Chatterjee, S., Christy, B., Cordes, J. M., Cornish, N. J., Crawford, F., Cromartie, H. T., Crowter, K., DeCesar, M. E., Demorest, P. B., Dolch, T., Ellis, J. A., Ferdman, R. D., Ferrara, E. C., Fonseca, E., Garver-Daniels, N., Gentile, P. A., Halmrast, D., Huerta, E. A., Jenet, F. A., Jessup, C., Jones, G., Jones, M. L., Kaplan, D. L., Lam, M. T., Lazio, T. J. W., Levin, L., Lommen, A., Lorimer, D. R., Luo, J., Lynch, R. S., Madison, D., Matthews, A. M., McLaughlin, M. A., McWilliams, S. T., Mingarelli, C., Ng, C., Nice, D. J., Pennucci, T. T., Ransom, S. M., Ray, P. S., Siemens, X., Simon, J., Spiewak, R., Stairs, I. H., Stinebring, D. R., Stovall, K., Swiggum, J. K., Taylor, S. R., Vallisneri, M., van Haasteren, R., Vigeland, S. J., and and, W. Z. (2018). *The NANOGrav 11-year data set: High-precision timing of 45 millisecond pulsars, The Astrophys. J. Suppl. Ser.* **235**, 2, pp. 37.

Baiotti, L. and Rezzolla, L. (2017). *Binary neutron star mergers: a review of einstein's richest laboratory, Reports on Progress in Physics* **80**, 9, pp. 096901.

Banik, S., Hempel, M., and Bandyopadhyay, D. (2014). *New Hyperon Equations of State for Supernovae and Neutron Stars in Density-Dependent Hadron Field Theory, Astrophys. J. Suppl. Ser.* **214**, 2, p. 22.

Baumgarte, T. W., Shapiro, S. L., and Shibata, M. (2000). *On the maximum mass of differentially rotating neutron stars, Astrophys. J.* **528**, 1, pp. L29–L32.

Bauswein, A., Bastian, N.-U. F., Blaschke, D. B., Chatziioannou, K., Clark, J. A., Fischer, T., and Oertel, M. (2019). *Identifying a first-order phase transition in neutron-star mergers through gravitational waves, Phys. Rev. Lett.* **122**, p. 061102.

Baym, G. and Chin, S. (1976). *Can a neutron star be a giant mit bag? Physics Letters B* **62**, 2, pp. 241–244.

Baym, Gordon and Hatsuda, Tetsuo and Kojo, Toru and Powell, Philip D. and Song, Yifan and Takatsuka, Tatsuyuki (2018). *From hadrons to quarks in neutron stars: a review, Rept. Prog. Phys.* **81**, 5, pp. 056902.

Becker, W. (2009). *Neutron Stars and Pulsars*, Astrophysics and Space Science Library (Springer, Berlin Heidelberg).

Blaschke, D. and Chamel, N. (2018). *Phases of Dense Matter in Compact Stars* (Springer International Publishing, Cham), ISBN 978-3-319-97616-7, pp. 337–400.

Boguta, J. (1982). *Baryonic degrees of freedom leading to density isomers, Phys. Lett. B* **109**, 4, pp. 251–254.

Boguta, J. and Bodmer, A. R. (1977). *Relativistic calculation of nuclear matter and the nuclear surface, Nucl. Phys. A* **292**, pp. 413.

Bonanno, Luca and Sedrakian, Armen (2012). *Composition and stability of hybrid stars with hyperons and quark color-superconductivity, A&A* **539**, pp. A16.

Buballa, M. (2005). *Njl-model analysis of dense quark matter, Phys. Rept.* **407**, 4-6, pp. 205–376.

Burgio, G. and Plumari, S. (2008). *Structure of hybrid protoneutron stars within the nambu-jona-lasinio model, Phys. Rev. D* **77**, 8, pp. 085022.

Burrows, A. and Vartanyan, D. (2021). *Core-collapse supernova explosion theory, Nature* **589**, pp. 29–39.

Butterworth, E. M. and Ipser, J. R. (1976). *On the structure and stability of rapidly rotating fluid bodies in general relativity. I. The numerical method for computing structure and its application to uniformly rotating homogeneous bodies. Astrophys. J.* **204**, pp. 200–223.

Cai, B.-J., Fattoyev, F. J., Li, B.-A., and Newton, W. G. (2015). *Critical density and impact of* $\Delta(1232)$ *resonance formation in neutron stars, Phys. Rev. C* **92**, pp. 015802

Camelio, G., Lovato, A., Gualtieri, L., Benhar, O., Pons, J., and Ferrari, V. (2017). *Evolution of a proto-neutron star with a nuclear many-body equation of state: Neutrino luminosity and gravitational wave frequencies, Phys. Rev. D* **96**, pp. 043015.

Chandrasekhar, S. (1970). *Solutions of two problems in the theory of gravitational radiation, Phys. Rev. Lett.* **24**, pp. 611–615.

Chapline, G. and Nauenberg, M. (1977). *Asymptotic freedom and the baryon-quark phase transition, Phys. Rev. D* **16**, pp. 450–456.

Chen, Y., Yuan, Y., and Liu, Y. (2009). *Neutrino mean free path in neutron star matter with* Δ *isobars, Phys. Rev. C* **79**, pp. 055802.

Chirenti, C., Miller, M. C., Strohmayer, T., and Camp, J. (2019). *Searching*

for hypermassive neutron stars with short gamma-ray bursts, Astrophys. J.
884, 1, pp. L16.

Demorest, P., Pennucci, T., Ransom, S., Roberts, M., and Hessels, J. (2010).
Shapiro Delay Measurement of A Two Solar Mass Neutron Star, Nature
467, pp. 1081–1083.

Dexheimer, V. and Schramm, S. (2008). *Proto–neutron and neutron stars in a*
chiral SU(3) model, Astrophys. J. **683**, 2, pp. 943–948.

Dolan, L. and Jackiw, R. (1974). Symmetry behavior at finite temperature, *Phys.*
Rev. D **9**, pp. 3320–3341.

Drago, A., Lavagno, A., Pagliara, G., and Pigato, D. (2014). *Early appearance of*
Δ *isobars in neutron stars, Phys. Rev. C* **90**, pp. 065809.

Duez, M. D. and Zlochower, Y. (2018). *Numerical relativity of compact binaries*
in the 21st century, Rep. Prog. Phys. **82**, 1, p. 016902.

Faber, J. A. and Rasio, F. A. (2012). *Binary neutron star mergers, Living Reviews*
in Relativity **15**, 1, p. 8.

Falcke, H. and Rezzolla, L. (2014). *Fast radio bursts: the last sign of supramassive*
neutron stars, A&A **562**, pp. A137.

Fechner, W. B. and Joss, P. C. (1978). *Quark Stars with 'Realistic' Equations of*
State, Nature **274**, pp. 347–349.

Fischer, T., Whitehouse, S. C., Mezzacappa, A., Thielemann, F. K., and Lien-
bendörfer, M. (2010). *Protoneutron star evolution and the neutrino-driven*
wind in general relativistic neutrino radiation hydrodynamics simulations,
A&A **517**, pp. A80.

Foglizzo, T. (2016). *Explosion Physics of Core-Collapse Supernovae* (Springer
International Publishing, Cham), pp. 1–21.

Friedman, E. and Gal, A. (2021). *Constraints on* Ξ^- *nuclear interactions from*
capture events in emulsion, Phys. Lett. B **820**, pp. 136555.

Friedman, J. L. (1983a). *Upper limit on the frequency of fast pulsars, Phys. Rev.*
Lett. **51**, pp. 718–718.

Friedman, J. L. (1983b). *Upper limit on the frequency of pulsars, Phys. Rev. Lett.*
51, pp. 11–14.

Friedman, J. L. (2018). *Gravitational-wave astrophysics from neutron star inspiral*
and coalescence, Int. J. Mod. Phys. D **27**, 11, 1843018.

Friedman, J. L., Ipser, J. R., and Parker, L. (1986). *Rapidly Rotating Neutron*
Star Models, Astrophys. J. **304**, pp. 115.

Fritzsch, H., Gell-Mann, M., and Leutwyler, H. (1973). *Advantages of the color*
octet gluon picture, Physics Letters B **47**, 4, pp. 365–368.

Fuchs, C., Lenske, H., and Wolter, H. H. (1995). *Density dependent hadron field*
theory, Phys. Rev. C **52**, pp. 3043–3060.

Fuentes, J. R., Espinoza, C. M., Reisenegger, A., Shaw, B., Stappers, B. W.,
and Lyne, A. G. (2017). The glitch activity of neutron stars, *A&A* **608**, p.
A131.

Fukushima, K. and Hatsuda, T. (2011). *The phase diagram of dense QCD, Rept.*
Prog. Phys. **74**, pp. 014001.

Fukushima, K. and Sasaki, C. (2013). *The phase diagram of nuclear and quark*
matter at high baryon density, Prog. Part. Nucl. Phys. **72**, pp. 99–154.

Garcia, F., Ranea-Sandoval, I. F. (2015). *A simple mechanism for the anti-glitch observed in AXP 1E 2259+586. Mon. Not. R. Astron. Soc.* **449**, pp. L73–L76.

Glendenning, N. K. (2012). *Compact Stars: Nuclear Physics, Particle Physics and General Relativity*, Astronomy and Astrophysics Library (Springer, New York).

Glendenning, N. K. (1985). *Neutron stars are giant hypernuclei?, Astrophys. J.* **293**, pp. 470–493.

Glendenning, N. K. and Weber, F. (1992). Nuclear Solid Crust on Rotating Strange Quark Stars, *Astrophys. J.* **400**, p. 647.

Hanauske, M., Bovard, L., Most, E., Papenfort, J., Steinheimer, J., Motornenko, A., Vovchenko, V., Dexheimer, V., Schramm, S., and Stöcker, H. (2019a). *Detecting the hadron-quark phase transition with gravitational waves, Universe* **5**, 6.

Hanauske, M., Steinheimer, J., Motornenko, A., Vovchenko, V., Bovard, L., Most, E. R., Papenfort, L. J., Schramm, S., and Stöcker, H. (2019b). *Neutron star mergers: Probing the eos of hot, dense matter by gravitational waves, Particles* **2**, 1, pp. 44–56.

Hartle, J. (1973). *Slowly Rotating Relativistic Stars. IX: Moments of Inertia of Rotationally Distorted Stars, Astrophys. and Space Sci.* **24**, pp. 385–405.

Hatsuda, T. and Kunihiro, T. (1994). Qcd phenomenology based on a chiral effective lagrangian, *Phys. Rept.* **247**, 5, pp. 221–367.

Hofmann, F., Keil, C. M., and Lenske, H. (2001). *Application of the density dependent hadron field theory to neutron star matter, Phys. Rev. C* **64**, pp. 025804.

Huber, H., Weber, F., Weigel, M. K., and Schaab, C. (1998). *Neutron Star Properties with Relativistic Equations of State, Int. J. Mod. Phys. E* **7**, 3, pp. 301–339.

Hüdepohl, L., Müller, B., Janka, H.-T., Marek, A., and Raffelt, G. G. (2010). *Neutrino signal of electron-capture supernovae from core collapse to cooling, Phys. Rev. Lett.* **104**, pp. 251101.

Itoh, N. (1970). *Hydrostatic Equilibrium of Hypothetical Quark Stars, Prog. Theor. Phys.* **44**, pp. 291.

Ivanenko, D. D. and Kurdgelaidze, D. F. (1965). *Hypothesis concerning quark stars, Astrophysics* **1**, pp. 251–252.

Janka, H.-T. (2012). *Explosion mechanisms of core-collapse supernovae, Ann. Rev. Nucl. Part. Sci.* **62**, 1, pp. 407–451.

Kajantie, K., Kärkkäinen, L., and Rummukainen, K. (1991). *Tension of the interface between two ordered phases in lattice su(3) gauge theory, Nucl. Phys. B* **357**, 2, pp. 693–712.

Ke, W. and Liu, Yu-xin (2014). *Interface tension and interface entropy in the 2+1 flavor Nambu-Jona-Lasinio model, Phys. Rev. D* **89**, p. 074041.

Keister, B. and Kisslinger, L. (1976). *Free-quark phases in dense stars, Phys. Lett. B* **64**, 1, pp. 117–120.

Klevansky, S. P. (1992). *The nambu—jona-lasinio model of quantum chromodynamics, Rev. Mod. Phys.* **64**, pp. 649–708.

Kolomeitsev, E., Maslov, K., and Voskresensky, D. (2017). *Delta isobars in relativistic mean-field models with σ–scaled hadron masses and couplings, Nucl. Phys. A* **961**, pp. 106–141.

Lattimer, J. M. and Steiner, A. W. (2014). *Constraints on the symmetry energy using the mass-radius relation of neutron stars, The Eur. Phys. J. A* **50**, 2, p. 40.

Lavagno, A. (2010). *Hot and dense hadronic matter in an effective mean-field approach, Phys. Rev. C* **81**, pp. 044909.

Li, J. J., Sedrakian, A., and Weber, F. (2018). *Competition between delta isobars and hyperons and properties of compact stars, Phys. Lett. B* **783**, pp. 234–240.

Lin, Z., Bratton, E., Weber, F., Orsaria, M. G., and Ranea-Sandoval, I. F. (2021). *Gravitational radiation-reaction driven instabilities in rotating neutron stars, Astron. Nachr.* **342**, pp. 799–807.

Lindblom, L. (1986). *Estimates of the maximum angular velocity of rotating neutron stars, Astrophys. J.* **303**, pp. 146.

Lindblom, L. and Detweiler, S. L. (1977). *On the secular instabilities of the Maclaurin spheroids. Astrophys. J.* **211**, pp. 565–567.

Lugones, G., Grunfeld, A. G., Ajmi, M. A. (2013). *Surface tension and curvature energy of quark matter in the Nambu-Jona-Lasinio model, Phys. Rev. C* **88**, p. 045803.

Lynch, R. S. *et al.* (2013). *The Green Bank Telescope 350 MHz Drift-scan Survey II: Data Analysis and the Timing of 10 New Pulsars, Including a Relativistic Binary, Astrophys. J.* **763**, p. 81.

Lyne, A. G. (1992). Glitches as probes of neutron star interiors, *Philosophical Transactions: Physical Sciences and Engineering* **341**, 1660, pp. 29–37.

Malfatti, G., Orsaria, M. G., Contrera, G. A., Weber, F., and Ranea-Sandoval, I. F. (2019). *Hot quark matter and (proto-) neutron stars, Phys. Rev. C* **100**, p. 015803.

Malfatti, G. (2020). *Non-local quark models for description of dense matter in the cores of neutron stars*, Ph.D. thesis, La Plata U., doi:10.35537/10915/107749, `arXiv:2010.14728 [nucl-th]`.

Malfatti, G., Orsaria, M. G., Ranea-Sandoval, I. F., Contrera, G. A., and Weber, F. (2020). *Delta baryons and diquark formation in the cores of neutron stars, Phys. Rev. D* **102**, pp. 063008.

Manchester, R. (2017). Pulsar glitches, *Proceedings of the International Astronomical Union* **13**, pp. 197–202.

Mariani, M., Orsaria, M., and Vucetich, H. (2017). *Constant entropy hybrid stars: a first approximation of cooling evolution, A&A* **601**, pp. A21.

Mariani, M. (2020). *Estrellas híbridas aisladas: criterios de estabilidad en modelos de proto-estrellas de neutrones y magnetares*, Ph.D. thesis, Universidad Nacional de La Plata, Argentina.

Maslov, K., Kolomeitsev, E., and Voskresensky, D. (2016). *Relativistic mean-field models with scaled hadron masses and couplings: Hyperons and maximum neutron star mass, Nucl. Phys. A* **950**, pp. 64–109.

Mastrano, A., Suvorov, A. G., Melatos, A. (2015). *Interpreting the AXP 1E*

2259+586 antiglitch as a change in internal magnetization. Mon. Not. R. Astron. Soc. **453**, pp. 522-–530.

Mezzacappa, A. (2005). *Ascertaining the core collapse supernova mechanism: The state of the art and the road ahead, Ann. Rev. Nucl. Part. Sci.* **55**, 1, pp. 467–515.

Misner, C. W., Thorne, K. S., and Wheeler, J. A. (1973). *Gravitation* (Freeman and Company, San Francisco).

Miyatsu, T., Cheoun, M.-K., and Saito, K. (2013). *Equation of state for neutron stars in su(3) flavor symmetry, Phys. Rev. C* **88**, pp. 015802.

Montoli, A., Pizzochero, P. M., and Antonelli, M. (2022). *Insight into the physics of neutron star interiors from pulsar glitches*, Astrophysics in the XXI Century with Compact Stars (World Scientific), ISBN 978-9-811-22093-7, (in press).

Most, E. R., Papenfort, L. J., Dexheimer, V., Hanauske, M., Schramm, S., Stöcker, H., and Rezzolla, L. (2019). *Signatures of quark-hadron phase transitions in general-relativistic neutron-star mergers, Phys. Rev. Lett.* **122**, p. 061101.

Oertel, M., Hempel, M., Klähn, T., and Typel, S. (2017). *Equations of state for supernovae and compact stars, Rev. Mod. Phys.* **89**, p. 015007.

Oppenheimer, J. R. and Volkoff, G. M. (1939). *On massive neutron cores, Phys. Rev.* **55**, pp. 374–381.

Orsaria, M., Rodrigues, H., Weber, F., and Contrera, G. A. (2013). *Quark-hybrid matter in the cores of massive neutron stars, Phys. Rev.* **D8**, 2, pp. 023001.

Orsaria, M., Rodrigues, H., Weber, F., and Contrera, G. A. (2014). *Quark deconfinement in high-mass neutron stars, Phys. Rev.* **C89**, 1, pp. 015806.

Orsaria, M. G., Malfatti, G., Mariani, M., Ranea-Sandoval, I. F., García, F., Spinella, W. M., Contrera, G. A., Lugones, G., and Weber, F. (2019). *Phase transitions in neutron stars and their links to gravitational waves, J. Phys. G: Nucl. Part. Phys.* **46**, 7, pp. 073002.

Owen, B. J., Lindblom, L., Cutler, C., Schutz, B. F., Vecchio, A., and Andersson, N. (1998). *Gravitational waves from hot young rapidly rotating neutron stars, Phys. Rev. D* **58**, pp. 084020.

Page, D., Geppert, U., and Weber, F. (2006). *The cooling of compact stars, Nucl. Phys. A* **777**, pp. 497–530,

Page, D. and Reddy, S. (2006). *Dense Matter in Compact Stars: Theoretical Developments and Observational Constraints, Ann. Rev. Nucl. Part. Sci.* **56**, 1, pp. 327–374.

Pandharipande, V. (1971). *Hyperonic matter, Nucl. Phys. A* **178**, 1, pp. 123–144.

Paschalidis, V. and Stergioulas, N. (2017). *Rotating stars in relativity, Living Reviews in Relativity* **20**, 1, p. 7,

Perego, Albino, Bernuzzi, Sebastiano, and Radice, David (2019). *Thermodynamics conditions of matter in neutron star mergers, Eur. Phys. J. A* **55**, 8, pp. 124.

Pons, J. A., Reddy, S., Prakash, M., Lattimer, J. M., and Miralles, J. A. (1999). *Evolution of Proto-Neutron Stars, Astrophys. J.* **513**, pp. 780–804.

Prakash, M., Bombaci, I., Prakash, M., Ellis, P. J., Lattimer, J. M., and Knorren,

R. (1997). *Composition and structure of protoneutron stars, Physics Reports* **280**, 1, pp. 1–77.

Rezzolla, L. and Olindo, Z. (2013). *Relativistic Hydrodynamics* (Oxford University Press).

Rezzolla, L., Pizzochero, P., Jones, D., Rea, N., and Vidaña, I. (2019). *The Physics and Astrophysics of Neutron Stars*, Astrophysics and Space Science Library (Springer International Publishing).

Riek, F., Lutz, M. F. M., and Korpa, C. L. (2009). *Photoabsorption off nuclei with self-consistent vertex corrections, Phys. Rev. C* **80**, pp. 024902.

Rijken, T. A., Nagels, M. M., and Yamamoto, Y. (2010). *Baryon-Baryon Interactions: — Nijmegen Extended-Soft-Core Models —, Prog. Theor. Phys. Suppl.* **185**, pp. 14–71.

Sawyer, R. F. (1972). *Energy shifts of excited nucleons in neutron-star matter, Astrophys. J.* **176**, pp. 205–211.

Schaffner-Bielich, J. and Gal, A. (2000). *Properties of strange hadronic matter in bulk and in finite systems, Phys. Rev. C* **62**, pp. 034311.

Schürhoff, T., Schramm, S., and Dexheimer, V. (2010). *Neutron Stars with small Radii—The Role of δ Resonaces, Astrophys. J.* **724**, 1, pp. L74–L77.

Schwarzschild, K. (1916). *On the gravitational field of a sphere of incompressible fluid according to Einstein's theory, Sitzungsber. Preuss. Akad. Wiss. Berlin (Math. Phys.)* **1916**, pp. 424–434.

Sedrakian, A. (2007). *The physics of dense hadronic matter and compact stars, Prog. Part. Nucl. Phys.* **58**, 1, pp. 168–246.

Sedrakian, A., Li, J.-J., and Weber, F. (2022). *Hyperonization in Compact Stars*, Astrophysics in the XXI Century with Compact Stars (World Scientific), ISBN 978-9-811-22093-7, (in press).

Shao, G.-Y. (2011). *Evolution of proto-neutron stars with the hadron–quark phase transition, Phys. Lett. B* **704**, 4, pp. 343—346.

Shapiro, S. L. (2000). *Differential rotation in neutron stars: Magnetic braking and viscous damping, Astrophys. J.* **544**, 1, pp. 397–408.

Shapiro, S. L. and Teukolsky, S. A. (1983). *Black Holes, White Dwarfs, and Neutron Stars: The Physics of Compact Objects* (Wiley).

Shen, G., Horowitzn, C. J., and Teige, S. (2011). *A new equation of state for astrophysical simulations, Phys. Rev. C* **83**, pp. 035802.

Sotani, H., Yasutake, N., Maruyama, T., and Tatsumi, T. (2011). *Signatures of hadron-quark mixed phase in gravitational waves, Phys. Rev. D* **83**, p. 024014.

Spinella, W. M. (2017). *A Systematic Investigation of Exotic Matter in Neutron Stars*, Ph.D. thesis, Claremont Graduate University & San Diego State University.

Spinella, W. M. and Weber, F. (2020). *Dense Baryonic Matter in the Cores of Neutron Stars*, Topics on Strong Gravity, Chap. 4 (World Scientific), pp. 85–152.

Spinella, W. M., Weber, F., Orsaria, M. G., and Contrera, G. A. (2018). *Neutrino Emissivity in the Quark-Hadron Mixed Phase, Universe* **4**, 5, pp. 64.

Steiner, A., Prakash, M., and Lattimer, J. (2000). *Quark-hadron phase transitions*

in young and old neutron stars, Phys. Lett. B **486**, 3-4, pp. 239–248.

Steiner, A. W., Lattimer, J. M., and Brown, E. F. (2010). *The Equation of State from Observed Masses and Radii of Neutron Stars, Astrophys. J.* **722**, 1, pp. 33–54.

Strobel, K., Schaab, C., and Weigel, M. K. (1999). *Properties of non-rotating and rapidly rotating protoneutron stars, A&A* **350**, pp. 497–512.

Takami, K., Rezzolla, L., and Baiotti, L. (2015). *Spectral properties of the post-merger gravitational-wave signal from binary neutron stars, Phys. Rev. D* **91**, pp. 064001.

Tolman, R. C. (1939). *Static solutions of einstein's field equations for spheres of fluid, Phys. Rev.* **55**, pp. 364–373.

Tolos, L. and Fabbietti, L. (2020). *Strangeness in nuclei and neutron stars, Prog. Part. Nucl. Phys.* **112**, pp. 103770.

Typel, S. (2018). *Relativistic Mean-Field Models with Different Parametrizations of Density Dependent Couplings, Particles* **1**, 1, pp. 3–22.

Typel, S., Röpke, G., Klähn, T., Blaschke, D., and Wolter, H. H. (2010). *Composition and thermodynamics of nuclear matter with light clusters, Phys. Rev. C* **81**, 1, pp. 015803.

Weber, F. (1999). *Pulsars as Astrophysical Laboratories for Nuclear and Particle Physics (Series in High Energy Physics, Cosmology and Gravitation)* (CRC Press).

Weber, F. (2005). *Strange quark matter and compact stars, Prog. Part. Nucl. Phys.* **54**, pp. 193–288.

Weber, F. and Glendenning, N. K. (1992). *Application of the Improved Hartle Method for the Construction of General Relativistic Rotating Neutron Star Models, Astrophys. J.* **390**, pp. 541.

Weissenborn, S., Chatterjee, D., and Schaffner-Bielich, J. (2012). *Hyperons and massive neutron stars: Vector repulsion and su(3) symmetry, Phys. Rev. C* **85**, pp. 065802.

Yasutake, N., Łastowiecki, R., Benić, S., Blaschke, D., Maruyama, T., and Tatsumi, T. (2014). *Finite-size effects at the hadron-quark transition and heavy hybrid stars, Phys. Rev. C* **89**, pp. 065803.

Zhu, Z.-Y., Li, A., Hu, J.-N., and Sagawa, H. (2016). $\Delta(1232)$ *effects in density-dependent relativistic hartree-fock theory and neutron stars, Phys. Rev. C* **94**, pp. 045803.